International Journal of Greenhouse Gas Control 106 (2021) 103260

Contents lists available at ScienceDirect

International Journal of Greenhouse Gas Control

journal homepage: www.elsevier.com/locate/ijggc

Influence of reservoir-scale heterogeneities on the growth, evolution and migration of a CO_2 plume at the Sleipner Field, Norwegian North Sea

G.A. Williams [a,*], R.A. Chadwick [b]

[a] British Geological Survey, The Lyell Centre, Research Avenue South, Edinburgh, EH14 4AP, United Kingdom
[b] British Geological Survey, Environmental Science Centre, Keyworth, Notts, NG12 5GG. United Kingdom

ARTICLE INFO

Keywords:
CCS
CO_2 storage
Sleipner
CO_2 plume
Heterogeneity
Utsira sand
Seismic
Monitoring

ABSTRACT

New analysis of the baseline (pre-injection) seismic data at Sleipner has revealed large-scale, roughly north-trending, channelled 'fairways' at a range of stratigraphical levels in the Utsira Sand. The baseline data also reveal localised stratigraphical 'point discontinuities' within the reservoir, some of which show evidence of having provided vertical conduits for earlier natural gas flow. The repeat time-lapse seismic datasets, where finer details of reservoir geology are illuminated by the reflective CO_2, show smaller-scale, north-trending and sometimes sinuous channels within the larger channel fairways. They also show a number of vertical CO_2 pathways within the CO_2 plume, corresponding to the point discontinuities seen on the baseline data.

Reservoir flow models were set up with flow properties constrained only by the observed levels of CO_2 accumulation in the reservoir and the arrival time of CO_2 at the reservoir top just prior to the first repeat seismic survey in 1999. The initial model with laterally homogeneous sand units separated by thin semi-permeable mudstones achieved only a moderate match to the observed time-lapse seismic data. Subsequent flow models, progressively incorporating higher permeability vertical CO_2 pathways through the mudstones and large-scale channel fairways within the reservoir sands, yielded a progressive and marked improvement in the history-match of key CO_2 layers within the plume. Crucially, no layer-specific model calibration was employed to achieve this improvement.

New geophysical measurements from Utsira Sand core have recently become available. These measurements provide important constraints on rock physics models of CO_2 and brine mixtures in the Utsira Sand. An empirical Brie fluid mixing law for intermediate fluid saturations provides a good fit to the new laboratory data, allowing measurements of CO_2 saturation to be converted into seismic velocity. This rock physics model was used to convert CO_2 saturation distributions predicted by the most realistic reservoir model into a seismic velocity model of the CO_2 plume. Synthetic seismic reflectivity profiles generated using this velocity model show a striking resemblance to the observed time-lapse seismic data, both in terms of plume layer reflectivity and also of time-shifts within and beneath the CO_2 plume. This provides confidence in the fidelity of the preferred reservoir model solution.

These results represent a significant breakthrough in the understanding and modelling of CO_2 plume development at Sleipner. We emphasise that the improvements were brought about not by fine tuning reservoir properties to fit the observed time-lapse data, but simply by incorporating geological permeability features that can reasonably be inferred from the baseline seismic data.

1. Introduction

CO_2 separated from natural gas produced at the Sleipner field in the North Sea (Norwegian block 15/9) is being injected into the Utsira Sand, a regional saline aquifer of late Cenozoic age (Fig. 1). Injection commenced in 1996 (Baklid et al., 1996) at a constant rate of around 0.8 Mt/a, with around 18.5 million tonnes stored by 2020. The storage aquifer comprises mostly unconsolidated sand of high porosity (>30 %) and high permeability (>1 Darcy) and is generally in excess of 200 m thick in the Sleipner area. A number of thin intra-reservoir mudstones, typically 1–2 m thick, are evident from geophysical logs acquired in wells around Sleipner (Fig. 1), and play a crucial role in controlling

* Corresponding author.
E-mail address: gwil@bgs.ac.uk (G.A. Williams).

https://doi.org/10.1016/j.ijggc.2021.103260
Received 17 June 2020; Received in revised form 23 December 2020; Accepted 4 January 2021
Available online 23 January 2021

development of the CO_2 plume.

Time-lapse seismic 3D data suggest the CO_2 has accumulated in the reservoir as a multi-tiered plume comprising individual layers of CO_2 trapped beneath the thin mudstones (Fig. 2) that have acted as partial baffles to the upward flow of CO_2. It is evident that flow through the mudstones is via at least one vertical high permeability CO_2 pathway (Chadwick et al., 2004), but the exact mudstone by-pass mechanisms are currently unknown.

The Sleipner CO_2 plume has been intensively studied by a number of researchers focussing respectively on quantitative seismic analysis (e.g. Williams and Chadwick, 2012; Furre et al., 2015; White et al., 2018; Chadwick et al., 2019) and fluid flow simulation (e.g. Chadwick and Noy, 2010; Cavanagh, 2013; Cavanagh and Haszeldine, 2014; Zhu et al., 2015; Williams and Chadwick, 2017). These studies have focused mainly on the topmost CO_2 layer in the plume and have provided important insights into the progressive lateral spread of a growing buoyant CO_2 layer beneath a caprock with topographic relief.

Full 3D flow simulations of the whole Sleipner plume have been neglected of late with relatively few examples in the published literature. Lindeberg et al. (2001) and Van der Meer et al. (2000) published 3D flow models of the CO_2 plume which produced reasonable replications of the CO_2 plume as it was interpreted from the first time-lapse seismic datasets in 1999. Both models had homogenous sand units, with the shape of individual CO_2 layers controlled by arbitrarily adjusting the topography of the mudstone topseal to each layer. The models differed fundamentally in how they simulated upward flow of CO_2 through the reservoir. Lindeberg et al. (2001) had intra-reservoir mudstones with discrete holes through which the CO_2 migrated upwards, whereas Van der Meer et al. (2000) modelled a reservoir with semi-permeable mudstones.

The key processes controlling fluid flow in the reservoir as a whole, both horizontal and vertical, remain poorly understood. It is only recently that workers have explicitly incorporated sedimentary permeability heterogeneity within the reservoir sand. Williams and Chadwick (2017) and Cowton et al. (2018) have assessed the effects of high permeability channels within the topmost sand body in the reservoir and

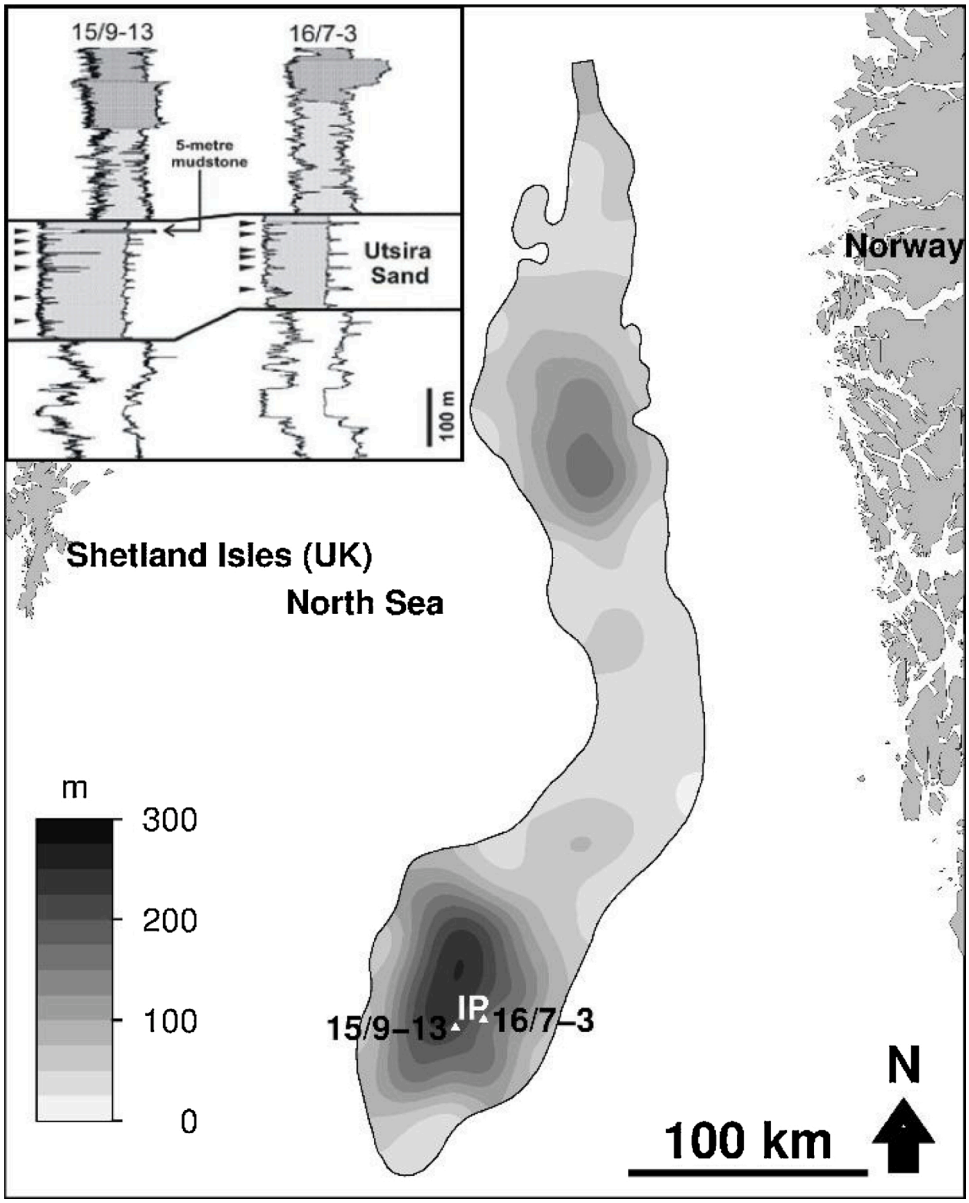

Fig. 1. Isopach map of the Utsira Sand and (inset) representative geophysical well logs showing reservoir heterogeneity (γ-ray logs on the left tracks and resistivity logs on the right tracks). The reservoir sand has characteristically low γ-ray and resistivity readings so peaks within the sand denote thin mudstones. The topmost reservoir sand unit lies above the 5-metre mudstone. IP = injection point.

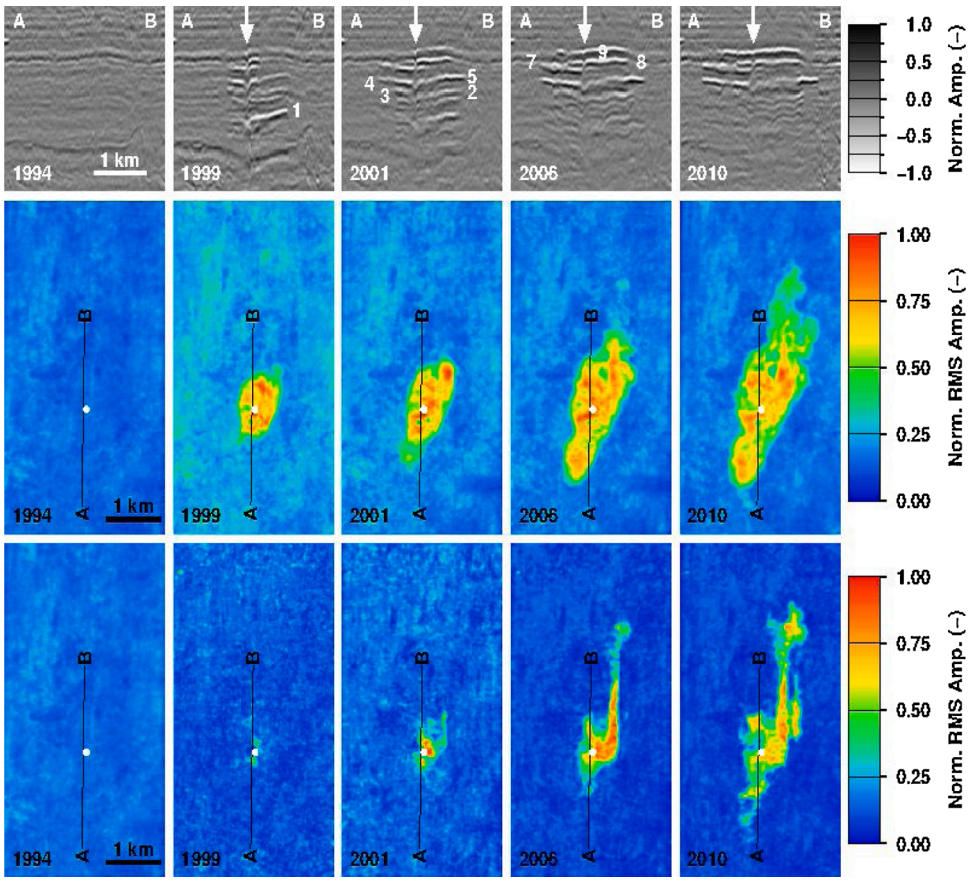

Fig. 2. Time-lapse 3D seismic data at Sleipner showing the 1994 baseline dataset and a selection of repeat surveys. Top: Seismic sections with strong CO_2 plume reflections, numbers referring to the individual CO_2 layers. Middle: Maps of whole plume reflectivity. Bottom: Maps of top CO_2 layer reflectivity. The main plume feeder chimney is indicated by an arrow on the seismic sections and by a white disc in map view.

shown how this enables an improved history-match. Detailed assessment of time-lapse seismic velocities and attributes (Chadwick et al., 2019), regional permeability, and wireline log data, also suggests that reservoir permeability is significantly heterogeneous, with zones of higher permeability associated with channelling significantly more prevalent than previously supposed. The precise nature of vertical fluid flow pathways through the reservoir remains enigmatic. They might reflect the lateral impersistence of the thin intra-reservoir mudstones, localised by-pass features due to sand injection, or even fractured gas chimneys. Irrespective of their exact morphology and geological origin, these are hereafter termed 'chimneys' for narrative simplicity.

The *modus operandi* of our paper is essentially a four-step process. First, we re-examine the baseline seismic data to see what inferences on medium- and large-scale channelling, vertical by-pass features and more distal mud-edifice features might be drawn from careful structural and stratigraphical interpretation of the baseline data. Second, we look for evidence of these features on the time-lapse seismic images, wherein they might be better illuminated by the reflective CO_2 (for example seismic chimneys). Third we investigate a range of putative permeability properties for these features by testing them via flow simulation against diagnostic aspects of the plume development such as the volumetric and spatial growth of key CO_2 layers within the plume. Finally, we carry out synthetic seismic modelling to test whether the proposed plume/reservoir structure is consistent overall with the time-lapse observations.

It is emphasised that detailed history-matching of individual layers within the Sleipner plume from the time-lapse seismic data is not the objective of this paper. Given the degree of parameter uncertainty in sand permeability and layer-seal topographies, we have elected to assess the nature of geologically realistic reservoir permeability heterogeneity and its influence on the broader development of a growing CO_2 plume.

2. Seismic observations of the CO_2 plume

The growth of the CO_2 plume has been monitored using time-lapse 3D seismic data, with a baseline survey in 1994, followed by repeats in 1999, 2001, 2002, 2004, 2006, 2008, and 2010 (Fig. 2). More recent surveys have also been acquired but these are not in the public domain. Here we do not focus on one particular survey or subset of surveys but rather select examples from the full span of released surveys in order to illustrate insights into plume characteristics.

The CO_2 plume is imaged on the seismic data as a number of high amplitude sub-horizontal reflections within the reservoir. Most of this reflectivity is thought to arise from thin layers of CO_2 trapped beneath the intra-reservoir mudstones which appear to be partially but not wholly sealing (Arts et al., 2008; Chadwick et al., 2004, 2005, 2010, 2015, 2016; see Saadatpoor et al., 2010 & Gershenzon et al., 2015 for a discussion of trapping mechanisms). The seismic data suggest that CO_2 has migrated vertically upwards through the reservoir via at least one chimney in the mudstones (Fig. 2) located a little to the south of the injection point. Locally up to nine interpreted reflective layers had formed by 1999 (when CO_2 first reached the top of the reservoir), and each individual reflective layer has been imaged on all of the subsequent surveys, although reflectivity of the deeper layers has decreased markedly with time (Figs. 2 and 3).

2.1. Seismic evidence for enhanced permeability pathways in the Utsira Sand

The time-lapse seismic data collected at Sleipner shows that CO_2 migration is being controlled by enhanced permeability pathways, both horizontal ('fairways') and vertical ('chimneys'). The reflection anomaly

from the whole CO_2 plume (Fig. 2) shows a pronounced N-S elongation with an aspect ratio of around 3:1, and, more specifically, the topmost layer of CO_2 (Fig. 2) has spread rapidly northward along a narrow topographic ridge in the reservoir topseal. Also, as mentioned above, there is evidence of vertical zones of enhanced permeability through which the CO_2 has bypassed the intra-reservoir mudstone baffles.

2.1.1. Seismic evidence for vertical permeability pathways (chimneys)

CO_2 in the Sleipner plume is trapped in discrete layers by a series of thin intra-reservoir mudstone baffles (Figs. 1 and 2). No data concerning the flow properties of these intra-reservoir mudstones are available. A Gas permeability (perpendicular to bedding) of between 3.5 and 5.5 $\times$ 10^{-7} Darcy was measured using a laboratory gas permeameter, on caprock core samples obtained from immediately above the top of the Utsira Sand (Harrington et al., 2010). The corresponding capillary entry pressures were in the range 1.6–1.9 MPa. The small buoyancy forces exerted by the CO_2 plume (Chadwick et al., 2012; Cavanagh, 2013) would be insufficient to drive CO_2 flow vertically upwards through a rock with these physical properties, which suggests that, in intact form, intra-reservoir mudstones with flow properties similar to the caprock samples would behave as capillary seals.

Seismic data suggest that the CO_2 has migrated vertically upwards through the reservoir and its intra-formational mudstones via a limited number of relatively permeable 'chimney' features, for example Chimneys 1, 2 and 3 (Fig. 4). Chimneys 1 and 3 correspond to subtle discontinuities in the stratigraphy, at or close to the top of the reservoir, and visible on the baseline (pre-injection) seismic data. Chimney 1 is particularly prominent on the repeat surveys where it is illuminated by CO_2 (Figs. 2 and 4), and is mappable as a distinctive vertical circular feature with a radius of about 30 m. It is interpreted as the main vertical conduit for CO_2 migration upwards through the plume and corresponds to the southerly of the two small accumulations of CO_2 which initially gathered at the top of the reservoir just prior to the 1999 seismic survey (Fig. 5), three years after the onset of injection (Chadwick et al., 2004). Chimney 3 shows on the baseline data as a distinctive stratigraphical break close to the reservoir top (Fig. 4a) and is indicated as a conduit for CO_2 in the Utsira Sand by the way in which more recent CO_2 accumulations have developed in the topmost reservoir sand body (Fig. 4b).

Chimney 2 corresponds roughly to the northern initial small accumulation of CO_2 at the top of the reservoir imaged in 1999 (Fig. 5). There is no direct evidence for this chimney on baseline seismic data, thus the presence of Chimney 2 is largely inferred by seismic observations of CO_2 layer growth on successive time-lapse volumes. It might be significant that this feature is close to the local structural culmination of the reservoir, where buoyant gas would be most likely to accumulate. Bright reflections in the overburden immediately above the chimney suggest the presence of methane gas. It is possible that the methane could have migrated from a deeper gas reservoir through the chimney into the overburden (Figs. 4b and 5 b), although there is no specific evidence to confirm this hypothesis.

Identifying sub-vertical features of limited spatial extent using seismic surveying techniques is extremely difficult. This is particularly true when the interval of interest (in this case the Utsira Sand interval) is seismically 'transparent', i.e. has limited internal reflectivity at the dominant wavelengths of the seismic survey. CO_2 injected at the Sleipner site has acted as a 'seismic tracer' allowing subtle stratigraphic features in the reservoir to be identified and mapped. Thus, the main feeder chimney (Chimney 1 in Fig. 4) is clearly imaged on successive seismic monitor surveys as a zone of chaotic low amplitude reflectivity cutting across the individual CO_2 reflections at a high angle. However, the presence of additional feeder chimneys is largely inferred from temporal and spatial variations in CO_2 layer growth. Consequently, there is inherent uncertainty in both the location and number of possible chimneys feeding CO_2 vertically through the reservoir. Furre et al. (2019) identified two additional small feeder chimneys 600 m to the north-east and 400 m to the south-west of Chimneys 2 and 3 respectively, based on careful seismic interpretation and amplitude mapping across successive seismic monitor surveys.

2.1.2. Seismic evidence for horizontal permeability pathways (fairways)

There is abundant seismic evidence for the development of enhanced permeability fairways at a range of scales in the Utsira Sand at Sleipner (Fig. 6). The highly reflective CO_2 plume is confined within a major channel fairway, flanked by topographic highs in the base reservoir surface (Fig. 6a). These topographic highs are variously interpreted as buoyant mud-rich diapirs (Zweigel et al., 2004) or sand injectites (Kennett, 2008) intruded into the reservoir from below. They are characterised by disruption of the overlying intra-reservoir reflections (Fig. 6b) and Kennett (2008) proposed that differential compaction due to fluid expulsion has down-folded intra-Utsira units onto these mounded features, a process that might well have reduced reservoir horizontal permeability. It is notable that the reservoir within the fairway between the two mound-like features is folded antiformally due to post-Utsira preferential compaction (Zweigel et al., 2004; Kennett, 2008). This interpretation is consistent with the buoyantly trapped CO_2 accumulations being spatially co-incident with the fairway formed between these mounds. A baseline seismic section (Fig. 6b) shows two diapirs with disrupted overlying reflectivity, a repeat section from 2010 showing the CO_2 plume confined within the upwarped region (Fig. 6c).

A detailed discussion pertaining to the depositional setting and sedimentology of the high permeability fairways is beyond the scope of this contribution. Gregersen and Michelsen (1997) suggest that the lower part of the Utsira Formation comprises a series of thick marine sand bodies, interpreted as stacked low-stand submarine fan deposits, while the upper part of the formation contains more clay and silt rich intervals, indicating increased relative sea level. A recent seismic-stratigraphic interpretation of the Utsira sequence in the vicinity the Sleipner CO_2 injection site (Kennett, 2008) concluded that the sand rich Utsira Formation was composed of largely south westerly dipping clinoforms, erosional scours, and large-scale sand waves, deposited in a high energy environment. Individual sandstone units are separated by thin (c.1.0–2.5 m thick), laterally discontinuous shale drapes, which have been eroded in places prior to the deposition of overlying sand units.

The presence of smaller scale channelling in the reservoir, oriented north-south, is revealed by an isochore map of the topmost reservoir sand wedge, between the 5-metre mudstone and the reservoir topseal (Fig. 7). A detailed stratigraphic study by the Norwegian Petroleum Directorate (Eidven et al., 2013) found that this sand layer is a separate stratigraphic unit, some 1 Ma younger than the Utsira Sand itself. The linear channel fairways are depositionally thicker than the surrounds, typically around 20 m thick, and correspond exactly to ridges in the topseal formed by later differential compaction. It is striking how closely the buoyantly migrating CO_2 in Layer 9 is trapped within the ridge topography.

Additional evidence for smaller scale channelling, albeit deeper in the reservoir, is afforded by Layer 2 where the CO_2 migration pattern illuminates a narrow N-S trending curvilinear channel fairway (Fig. 3) which is acting as a high flow thief zone, presumably of enhanced permeability.

3. Whole plume numerical flow simulations

3.1. Mesh design and rock properties

A geological model of the Utsira Sand reservoir was built using PETREL for modelling with the ECLIPSE 100 black oil simulator. The top and base of the reservoir were mapped from the baseline (1994) seismic dataset and depth-converted using a uniform mean overburden velocity of 1845 ms^{-1} and a reservoir velocity of 2050 ms^{-1}. The model was discretised horizontally into 60 cells in the X direction and 111 cells in the Y direction, with a cell size of 50 $\times$ 50 m (Fig. 8a). Vertically the

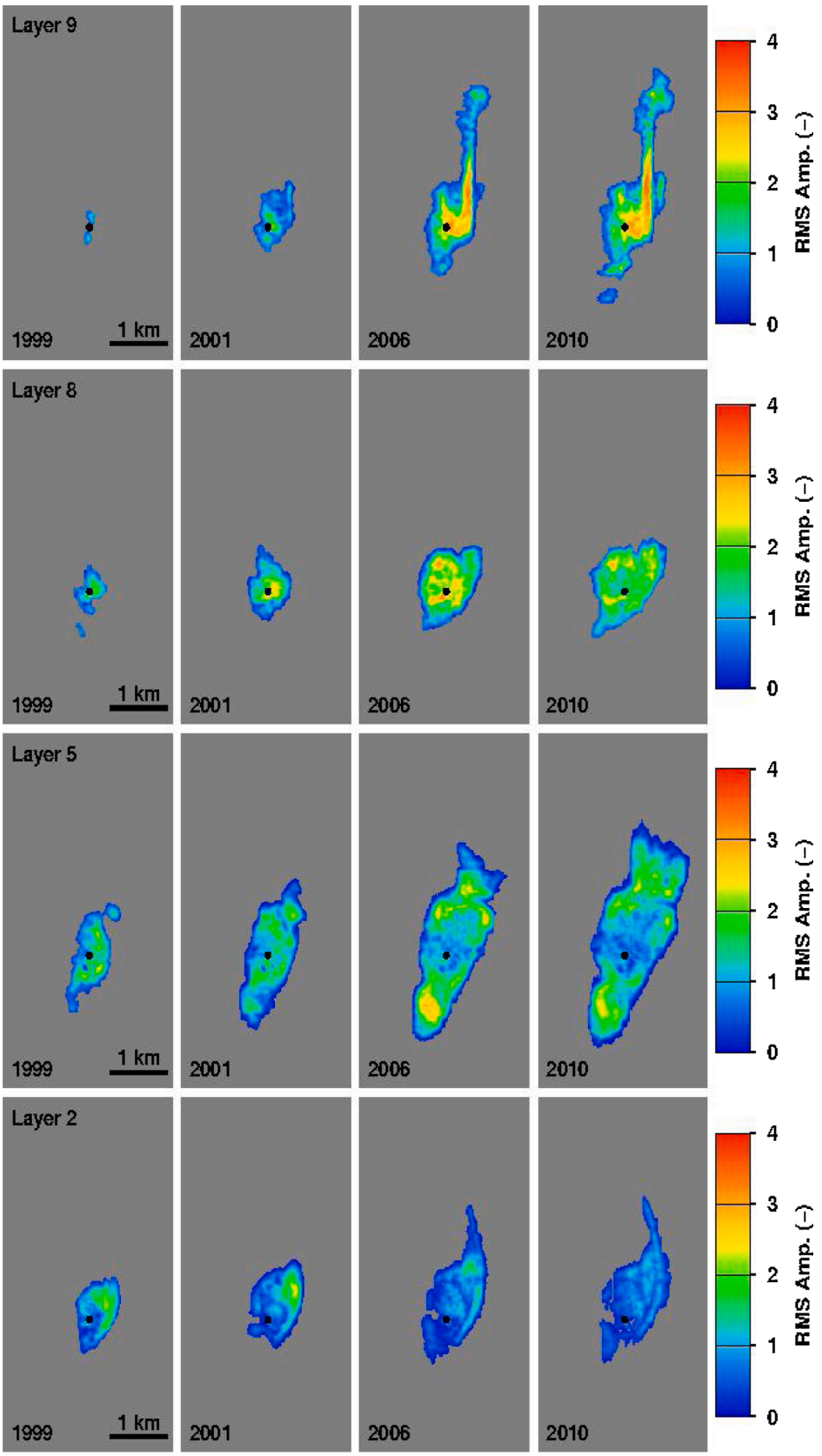

Fig. 3. Development of Layers 9, 8, 5 and 2 showing channelling (Layers 9 and 2) and stabilisation/dimming (Layer 2). The injection point (situated beneath the plume) is shown as a black disc.

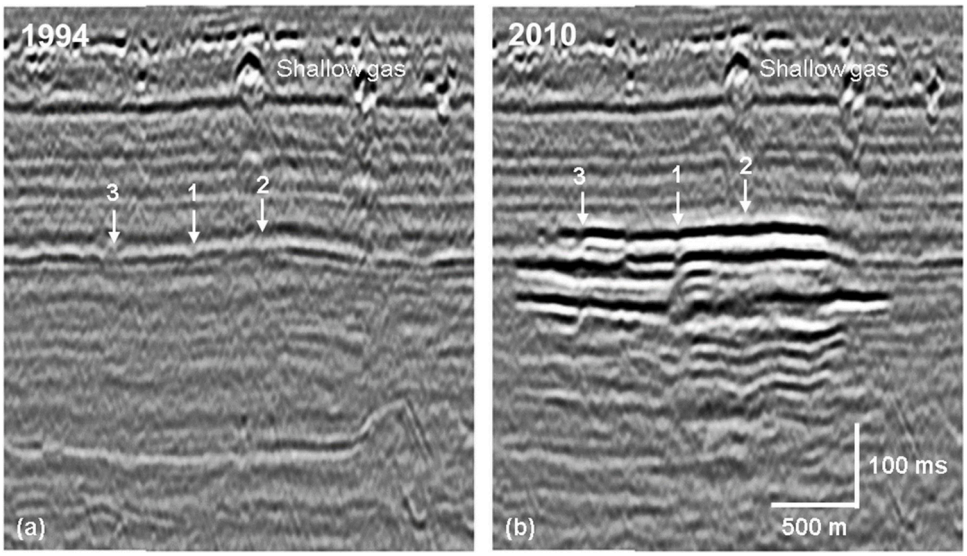

Fig. 4. Time-lapse seismic inline through the Sleipner CO_2 injection site showing the three putative 'chimneys' (arrowed). a) 1994 baseline data prior to the injection of CO_2. b) 2010 after fourteen years of injection.

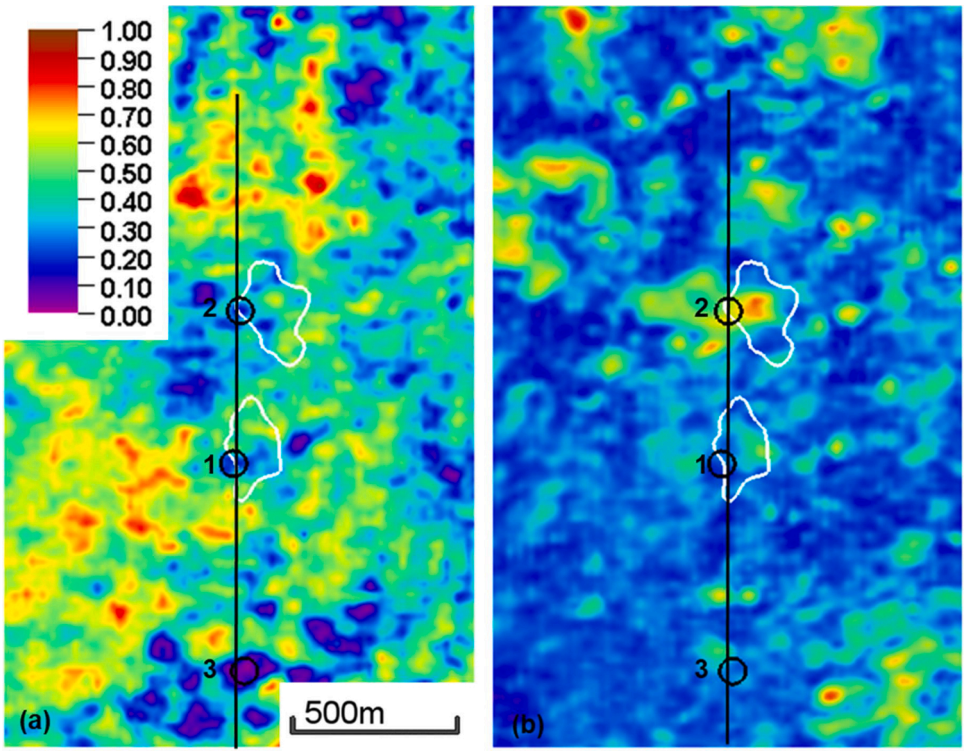

Fig. 5. a) Normalised absolute reflection amplitude from a 32 milli-second window about the top 5 m mudstone layer as imaged on the 1994 baseline seismic survey. The location of seismic chimneys 1 to 3 are shown as reduced amplitude zones, highlighted by black circles. b) Normalised RMS amplitude computed for the shallow gas layer labelled in Fig. 4. White polygons denote the extents of two accumulations of CO_2 developed at the top of the reservoir on the 1999 survey.

reservoir was discretised into 132 cells with a mean cell height of 2 m. No-flow boundary conditions were placed at the top and base of the reservoir (simulating an impermeable caprock and mudstone underburden), while the lateral boundary domains were maintained at near hydrostatic pressure conditions by using a large pore-volume multiplier.

The reservoir was sub-divided into a series of sand layers separated by thin mudstone horizons (Fig. 8b): rock properties for each layer are summarised in Table 1. The reservoir sands were assigned a porosity of 0.37 based on a mean of core and geophysical log measurements (Zweigel et al., 2004). Permeability data is scarce. Core-plug measurements from well N15/9-A23, are in the range 1.6–3.3 Darcy (Zweigel et al., 2004), but the well lies to the west of the CO_2 plume, above the flanks of a mud diapir and outwith the channel fairway occupied by the CO_2 plume. Based on this, a re-assessment of regional permeability and wireline log data (Williams and Chadwick, 2017) indicated that the Utsira Sand around the CO_2 plume is significantly more permeable than in the tested core material. Well test data from the Grane and Oseberg fields, north of Sleipner, yield permeability values of 5.8 and 1.1–8.14 Darcy respectively. Here we assign a permeability of 2 Darcy east-west (perpendicular to the bulk sediment transport direction)

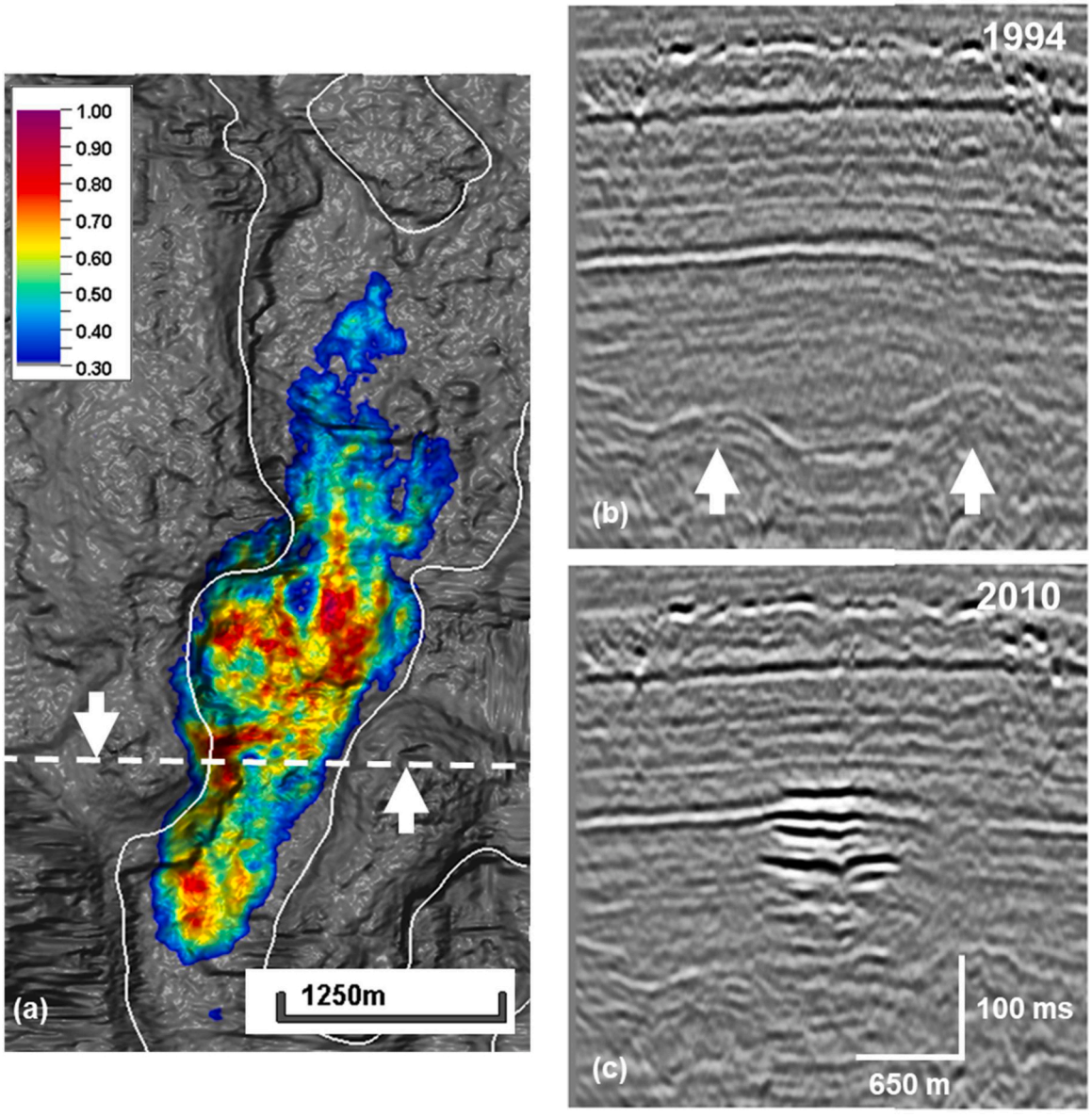

Fig. 6. Major channel fairway developed in the Utsira Sand at Sleipner. a) Zone of high amplitude CO_2 reflectivity (expressed as normalised absolute reflection amplitude) confined to the channel fairway flanked by topographic highs (arrowed) in the base reservoir surface. b) Seismic section (along the broken white line in (a)) from the 1994 baseline data through the channel and flanking highs. c) Same section from the 2010 survey. The white polygon in (a) represents the 1050 m depth contour, used to define the margins of the high permeability channel fairway incorporated into the lower sand units in the reservoir models described below.

and 8 Darcy north-south (parallel to the bulk sediment transport direction), values more in line with the well-test measurements.

The intra-reservoir mudstones can be identified by their high γ-ray response on wireline logs in the area (Fig. 1), but with the exception of Mudstone 8 they are not resolved on the seismic data and cannot be mapped directly. However, their approximate positions were aligned to the elevations of the reflective CO_2 layers in the plume and their topography constrained to be parallel to that of Mudstone 8. Seven mudstones were realised corresponding to the main reflections (CO_2 Layer 6 is laterally restricted and was not assigned a corresponding mudstone). Mudstone fluid transport properties were varied between simulations (Table 1) in order to investigate likely bypass mechanisms. Two categories of mudstone property were assumed: a low permeability 'intact' mudstone corresponding to the laboratory core test results and a 'semi-permeable' mudstone required to model the observed arrival of CO_2 at the top of the reservoir in 1999 (see below). Relative permeability and capillary pressure curves for CO_2 and brine were computed using a Van-Genuchten model (Table 1 and Fig. 9). The Utsira Sandstone curves (Fig. 9a) are based on laboratory measurements of core samples (Erik Lindeberg personal communication; Falcon-Suarez et al., 2018). No laboratory measurements were available for the mudstone layers, so values used previously by Chadwick and Noy (2010, 2015) have been adopted here.

It is noted that our model is geometrically very similar to the recently released Sleipner 2019 benchmark model (Equinor, 2020). It covers the same area as the Equinor model and differs from it principally in that it incorporates a range of additional horizontal and vertical permeability heterogeneity options. The benchmark model also integrates seismic interpretations of the upper shale reflectors (Mudstone 5–7 in Fig. 8b) derived from high resolution seismic imaging data acquired in 2010. Consequently, these layers differ morphologically from the current model. The distribution of the vertical feeder chimneys is also different to the 2019 Sleipner benchmark (Furre et al., 2019), although the position and geometry of the main CO_2 conduit (Chimney 1 in Fig. 4)

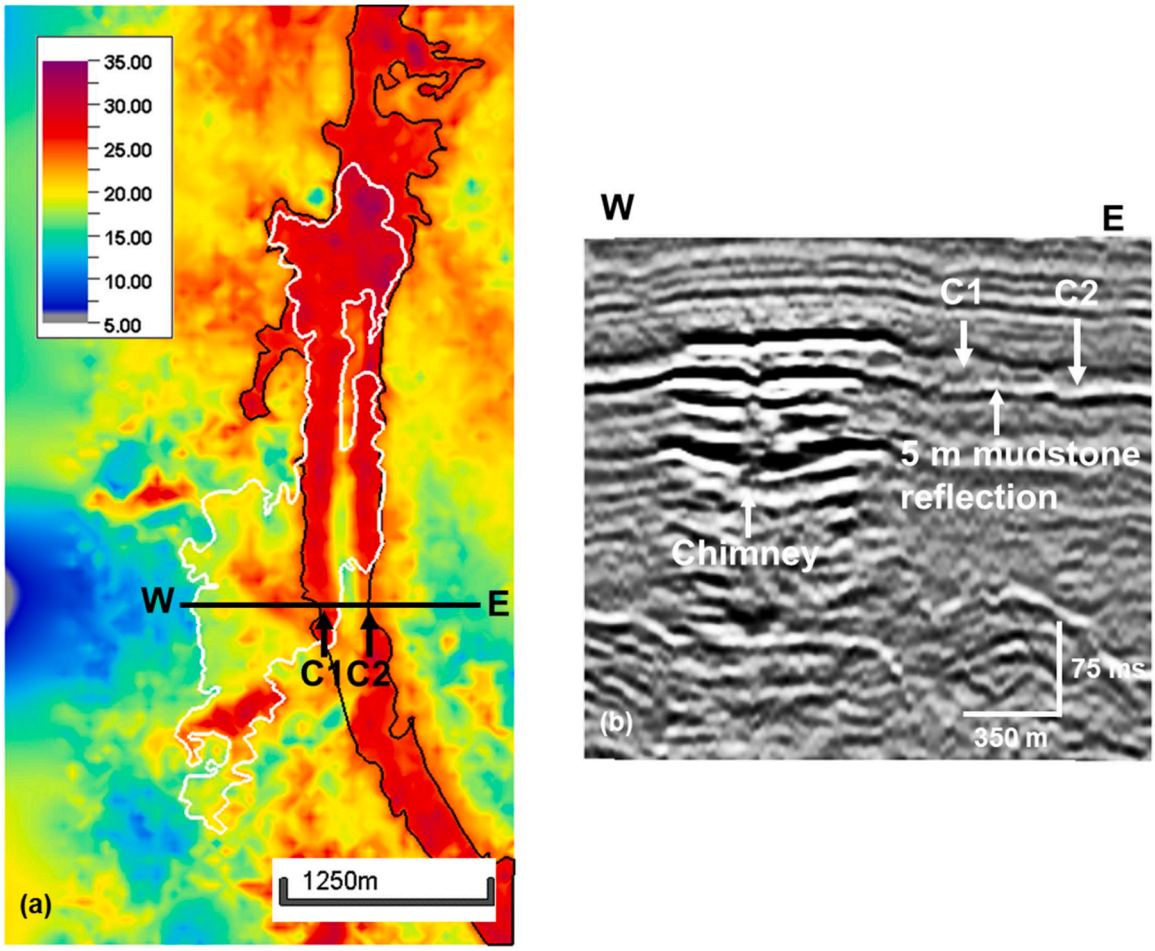

Fig. 7. a) Shaded isochore map (thickness in m) of the topmost sand unit. C1 and C2 are examples of individual channel fairways in the sand unit. The black polygon defines the margins of the high permeability channel fairway in the topmost sand unit in the reservoir models described below. The white polygon delineates the margins of the topmost CO_2 layer in 2010. The solid black line shows the location of the seismic section. b) High resolution seismic image in 2010 showing the topmost sand body together with CO_2 layers in the Utsira Sand. The 5-metre mudstone separates the topmost sand body from the main Utsira Sand beneath and this has been breached through a distinct chimney feature.

remains the same.

3.2. Fluid properties

The density and compressibility of CO_2 as a function of pressure were calculated for a mean reservoir temperature of 33 °C using the Span and Wagner (1996) equation-of-state (Table 2) and converted to the relevant black oil representation following the scheme published by Hassanzadeh et al. (2008). The viscosity of CO_2 was calculated as a function of temperature and density using relationships published by Vesovic et al. (1990) and Fenghour et al. (1998). Based on these correlations, the average density and viscosity of CO_2 in the reservoir was around 700 kg/m^3 and 6.0 $\times$ 10^{-5} Pa.s respectively.

The black oil approximation used in these simulations was considered valid for the purpose of this study. The Utsira reservoir has a mean thickness of 240 m in the Sleipner area. Incorporating a geothermal gradient of 31.7 C/km (Alnes et al., 2011) results in a temperature change of 7.5 C from the top to the base of the reservoir. This equates to a maximum change in CO_2 density of around 50 kg/m^3 and viscosity of 0.8 $\times$ 10^{-5} Pa.s compared to the values in Table 2. Previous modelling studies (Chadwick and Noy, 2010; Williams and Chadwick, 2017) suggest that this will not significantly change the modelled CO_2-water contacts.

There is some additional uncertainty regarding the temperature of CO_2 (and consequently fluid properties) in the Sleipner plume. The temperature of the CO_2 at the injection perforations is estimated at ~48 C (Alnes et al., 2011), around 13 C warmer than ambient reservoir temperature at the injection point. Furthermore, interpretation of the time-lapse gravity data (Alnes et al., 2011) suggest that the average density of the CO_2 plume at Sleipner is compatible with a warm, less dense, axial core.

The effects of a plume of warm buoyant CO_2 rising to the top of the reservoir have been investigated by Williams and Chadwick (2017). Numerical modelling showed an axial column of elevated fluid temperatures extending above the injection point to the top of the reservoir, undergoing Joule-Thomson cooling as the CO_2 expands. The thermal anomaly extends to a radius of around 350 m from the injection well, potentially reducing fluid density to around 400 Kg/m^3 in the core of the plume, which increases to around 730 kg/m^3 as the plume cools radially toward background reservoir temperatures (Williams and Chadwick, 2017). The corresponding dynamic viscosity ranges from 40 to 60 μPa.S. 3D numerical modelling suggests that the relatively localised increase in fluid mobility is insufficient to induce anything but a very minor increase in lateral spreading of the CO_2 layers (Williams and Chadwick, 2017), consequently, temperature effects have not been considered further in this contribution.

Brine is represented as an oil phase in the simulator allowing for CO_2 dissolution: the mean brine density without any dissolved CO_2 was 1024 kg/m^3 based on a salt mass fraction of 0.032. Activity coefficients for CO_2 and H_2O were obtained directly from the equation-of-state using the

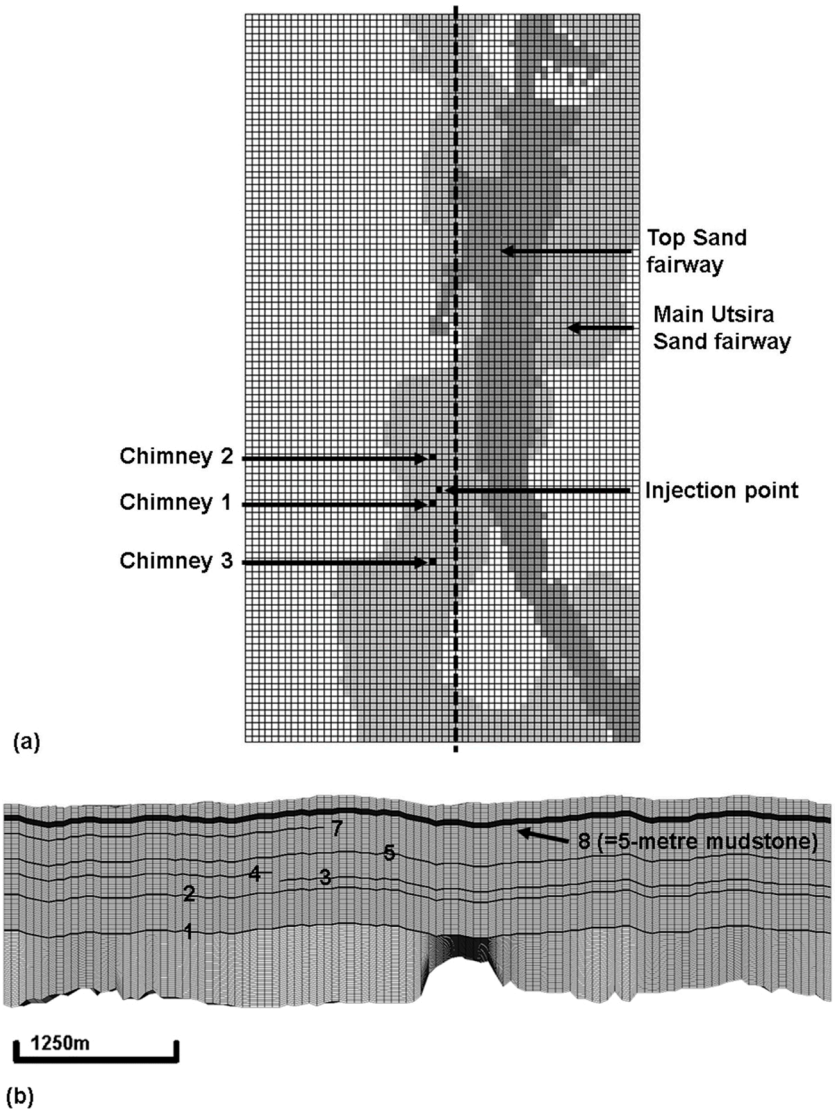

Fig. 8. (a) Reservoir model mesh showing the geometry of the two enhanced permeability fairways used in Models 7-10. The CO_2 injection point and the main feeder chimneys (Fig. 4) are also shown. (b) North-south cross-section through the reservoir model along the dashed line in (a). Individual mudstone layers are numbered upwards through the top of the reservoir, the numbers corresponding to those of the CO_2 layers trapped beneath them (Fig. 2). Note that CO_2 Layer 6 is laterally restricted and was not assigned a corresponding mudstone in the models.

Table 1
Rock units and physical properties used in the modelling.

Property	Low permeability mudstone	Semi-permeable mudstone	Sand
Porosity (-)	0.34	0.34	0.37
Permeability X (mD)	0.0001	100	2.0
Permeability Y (mD)	0.0001	100	8.0
Permeability Z (mD)	0.0001	100	2.0
Van Genuchten λ (-)	0.4	0.6	0.6
Slr (-)	0.2	0.05	0.05
Sgr (-)	0.0	0.0	0.0
Capillary entry pressure (Pa)	2.0×10^6	1.55×10^5	1.0×10^3

methodology described by Spycher and Pruess (2005), while the solubility of CO_2 in brine was calculated according to Duan et al. (2006). Brine density and viscosity were taken from the International Association for the Properties of Water and Steam tables, using Ezrokhi's method to calculate the density effect of salt and dissolved CO_2 (Zaytsev and Aseyev, 1992).

3.3. CO_2 injection rates

The CO_2 is injected via a deviated well (N15/9-A-16) in a dense phase at a depth of around 1012 m below sea level, approximately 200 m below the top of the aquifer, the length of the injection perforations being 38 m. Injection commenced in 1996 at a roughly constant rate, with around 18.5 million tons of CO_2 stored by 2020. The CO_2 was injected into three cells corresponding to the top perforated interval in the deviated well in the simulations. A variable injection rate with a mean value of 27 kgs^{-1} was used, based on the actual values measured at the wellhead (Fig. 9d, Ola Eiken personal communication).

3.4. CO_2 arrival and accumulation in the uppermost sand layer

The growth history of the topmost layer of CO_2 (Layer 9) places a key constraint on reservoir simulations of the whole plume. The lateral and vertical extent of this layer can be mapped with a high degree of precision using time-lapse seismic data (Figs. 2 and 10) and converted into volumetric estimates of layer growth (Fig. 11) by using structural mapping of the top reservoir surface and assuming a flat CO_2-water contact (the static ponding model) or a laboratory-determined capillary pressure–saturation relationship (the dynamic plume model): see Chadwick and Noy (2010) for methodology. Whole plume simulations are constrained by the need to match the observed arrival of CO_2 at the top of the reservoir just prior to the time of the 1999 seismic monitor survey (a very robust calibration), and also the volumetric growth of the layer over time.

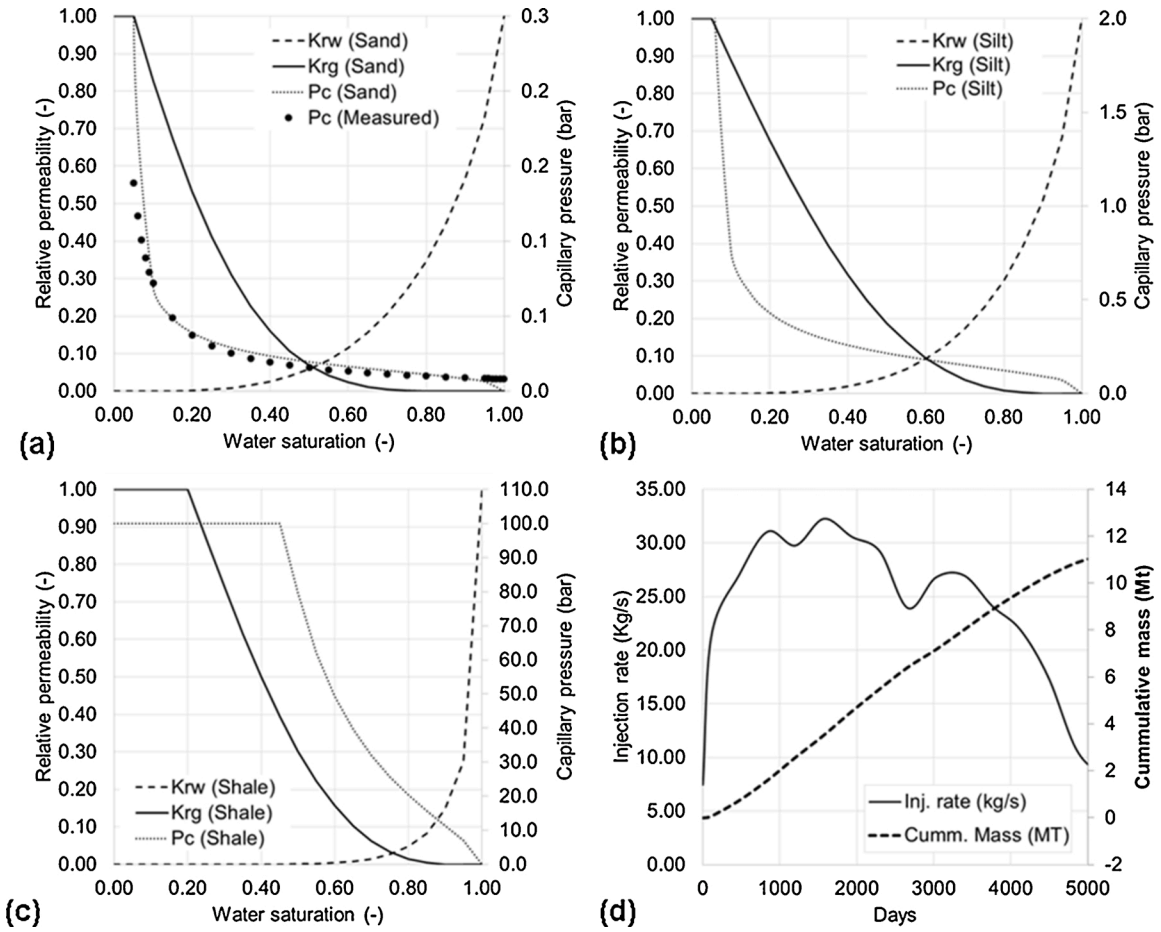

Fig. 9. (a) Relative permeability and capillary pressure curves for the Utsira Sand. (b) Relative permeability and capillary pressure curves used for assumed semi-permeable intra-reservoir mudstones. (c) Relative permeability and capillary pressure curves for assumed low permeability intact intra-reservoir mudstones. (d) Injection rate as a function of time.

Table 2
Representative CO_2 fluid properties used in the modelling.

Depth	Pressure (MPa)	Density (kg m^{-3})	Viscosity (x10^{-5} Pa s)
700	7.3	270.62	2.1690
750	7.8	551.21	3.9938
800	8.3	653.31	5.0272
850	8.8	689.82	5.4645
900	9.3	713.78	5.7753
950	9.8	732.04	6.0263
1000	10.3	746.98	6.2416
1050	10.8	759.73	6.4327
1100	11.3	770.89	6.6061

3.5. Simulation approach

The whole plume simulations were designed to investigate the distribution of vertical and horizontal permeability pathways in the Sleipner CO_2 plume and their role in its temporal evolution. Vertical pathways were represented by model chimneys. Up to three chimneys (Fig. 8a) were incorporated in the models, each formed by two 50 × 50 m grid cells emplaced in each mudstone layer, and giving a spatial footprint area of 5000 m^2. This is comparable with Chimney 1, as observed on seismic data, a roughly circular feature with a radius between 30 m and 60 m (Fig. 5), and a spatial footprint in the range 2840 - 11,300 m^2. Horizontal pathways were represented by higher permeability channel fairways in the reservoir sand layers (see below).

3.5.1. Homogeneous sand models

In the first six simulations (Models 1–6) the height, number and flow properties of the chimneys through the mudstones were systematically varied (Table 3). In these models the reservoir sands were assigned a permeability of 2 Darcy east-west and 8 Darcy north-south throughout the grid. Each intra-reservoir mudstone was assigned a permeability of either 100 mD (semi-permeable) or 0.0001 mD (low permeability) depending on the model. The semi-permeable mudstone value was derived from a series of initial runs of simulation Model 1 (Table 3) in which an assumed uniform mudstone permeability was adjusted to allow a small amount of CO_2 to reach the top of the reservoir just prior to the 1999 time-lapse repeat seismic survey. Relative permeability and capillary pressure curves for each rock type are shown in Fig. 9.

3.5.2. Channelled sand models

The subsequent four models (Models 7–10) incorporate two high permeability N-S channel fairways: one in the sand units of the main Utsira reservoir (Figs. 6 and 8a) and one in the topmost sand unit (Figs. 7 and 8a). The sands within these channels were again assigned a permeability of 2 Darcy east-west and 8 Darcy north-south. Outside the main channel fairway, properties corresponding to the semi-permeable mudstone (Table 1 and Fig. 9b) were assigned in Models 7, 8 and 9, whilst in Model 10 the reservoir permeability outside the channel fairway was increased by an order of magnitude to 1 Darcy. The topmost sand is separated from the main reservoir sands by the 5-metre mudstone and is assumed to be unaffected by the deeper mud intrusions (Figs. 6b and 7 b), so a permeability of 2 Darcy was assigned outside the channel. Capillary pressure and relative permeability curves

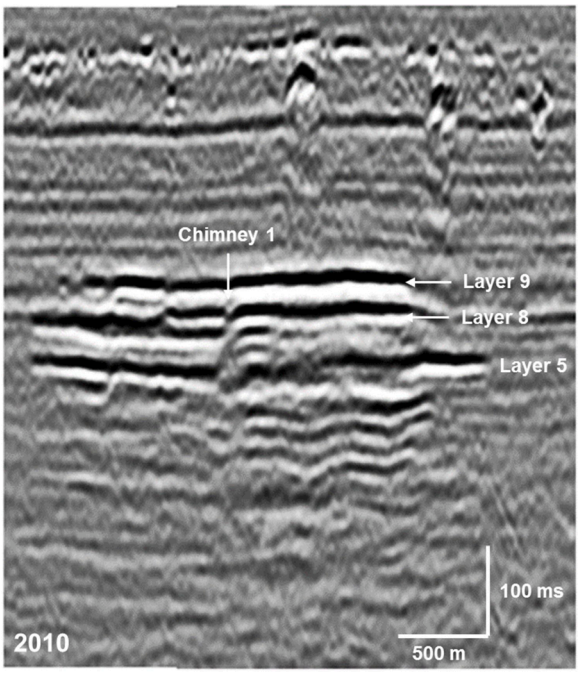

Fig. 10. Seismic line through the CO_2 plume in 2010. Reflections from the three main CO_2 layers that can be mapped accurately across successive time-lapse surveys are labelled. Chimney 1 is also prominent in the central part of the plume.

for the Utsira Sand (Fig. 9a) were used.

3.6. Simulation results

The time-lapse seismic data provide two key observational controls on flow model fidelity. First is the tightly constrained initiation of Layer 9 (the topmost CO_2 layer) just prior to the 1999 survey and its subsequent volumetric growth (Figs. 2 and 11). Second is the lateral spread of the deeper CO_2 layers in the plume. The largest of these are Layer 5 (beneath Mudstone 5), Layer 8 (beneath Mudstone 8) and Layer 9 (beneath the reservoir topseal). These layers have been mappable since the first repeat survey in 1999, continue to grow with time, and probably hold the bulk of trapped CO_2 in the plume (Fig. 10). It is clear therefore that matching the reservoir model to the observed spatial extents of these layers, through time, is a key modelling constraint.

The volumetric growth of the Layer 9, for each of the flow simulations (Table 3), is illustrated with reference to CO_2 volumes estimated from the time-lapse survey data (Fig. 11). Growth of this and the other key CO_2 layers is discussed for each model in more detail below.

3.6.1. Homogeneous sand models

3.6.1.1. Model 1. The simplest reservoir scenario is represented by Model 1 with uniform semi-permeable mudstones and no chimneys (Fig. 12). It produces the correct initiation time for Layer 9, but also gives a high and rapidly increasing flux of CO_2 into the top reservoir sand (Fig. 11). This is because the CO_2 flux steadily increases through the deeper mudstones as the spatial extents of the deeper CO_2 layers grow and their relative permeabilities increase with CO_2 saturation. As a consequence, the net rate of CO_2 accumulation increases with time in the shallower layers but diminishes (and may become negative) in the deeper layers. The fluid saturation profile (Fig. 12a) shows that most of the injected CO_2 has reached Layer 9 by 2008, and has spread laterally far beyond the CO_2 - Water Contact (CWC) as observed on the seismic (Fig. 12b). Although the footprint of Layer 8 shows quite good agreement with the seismic data (Fig. 12c), there is less CO_2 in the deeper plume layers, so Layer 5 is very much smaller than observed (Fig. 12d). Assigning a lower permeability (or higher capillary entry pressure) to the semi-permeable mudstone layers reduces the cumulative volume of CO_2 arriving at the top layer, but crucially also delays the arrival of CO_2 at this layer, and it is not otherwise possible to replicate the key observed arrival of CO_2 beneath the caprock just prior to the 1999 seismic survey.

3.6.1.2. Model 2. The opposite model end-member is provided by Model 2 (Fig. 13), with low permeability intra-reservoir mudstones cut by a single semi-permeable chimney, corresponding to Chimney 1 (Figs. 4 and 10). Unlike Model 1 the spatial extent of CO_2 layers accumulating beneath semi-permeable baffles does not grow with time and so any temporal increase of upward flux is limited to the increase of relative permeability with saturation. This is a minor effect, insufficient to replicate the growth of Layer 9 as observed on the seismic (Fig. 11 and 13b). Most of the modelled CO_2 is trapped within the deeper CO_2 layers (Fig. 13a) and the model does not remotely replicate the observed CWC for Layer 9 or Layer 5 (Fig. 13b and d). Adjusting the permeability and

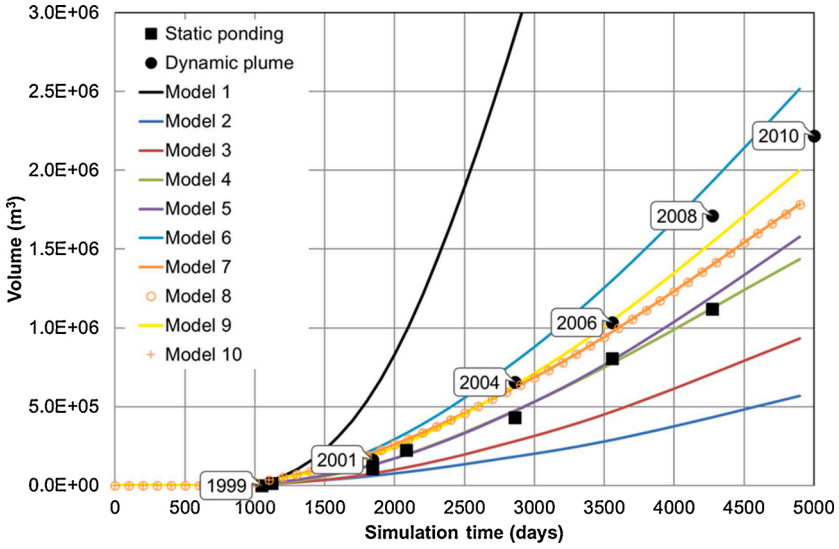

Fig. 11. Observed volumetric growth of Layer 9 (topmost CO_2 layer) compared with calculated layer volumes for each of the flow model scenarios (numbered for clarity). Note that all of the models produce the correct initiation time for the layer, just prior to the 1999 survey.

Table 3
Key permeabilities in milli-Darcy (mD) for each model run. Models 7-10 introduce two high permeability N-S channel fairways in the Utsira Sand (see Figs. 5 and 6). [1]In Model 9 Chimney 3 was assigned reservoir sand properties (Fig. 9a). [2]In Model 10 Chimney 3 was assigned reservoir sand properties at the level of Mudstone 5 and semi-permeable mudstone properties above this layer. White rows denote models with just mudstone property variation; grey rows include property variation associated with channel fairways developed in the sand units.

Model	Mst. 1 (mD)	Mst. 2 (mD)	Mst.3 (mD)	Mst. 4 (mD)	Mst. 5 (mD)	Mst. 7 (mD)	Mst. 8 = 5m mudstone (mD)	Number of channels	Channel sand permeability (mD)	Number of chimneys	Chimney permeability (mD)
1	100	100	100	100	100	100	100	Homogeneous	N/A	0	N/A
2	0.0001	0.0001	0.0001	0.0001	0.0001	0.0001	0.0001	Homogeneous	N/A	1	100
3	100	100	100	100	0.0001	0.0001	0.0001	Homogeneous	N/A	1	100
4	100	100	100	100	100	100	0.0001	Homogeneous	N/A	1	100
5	100	100	100	100	0.0001	0.0001	0.0001	Homogeneous	N/A	2	100/100
6	100	100	100	100	0.0001	0.0001	0.0001	Homogeneous	N/A	2	100/100
7	100	100	100	100	0.0001	0.0001	0.0001	2	2000/8000 (100 outside channel)	2	100/100
8	100	100	100	100	0.0001	0.0001	0.0001	2	2000/8000 (100 outside channel)	3	100/100/100
9	100	100	100	100	0.0001	0.0001	0.0001	2	2000/8000 (100 outside channel)	3	100/100/1000[1]
10	100	100	100	100	0.0001	0.0001	0.0001	2	2000/8000 (1000 outside channel)	3	100/100/100-1000[2]

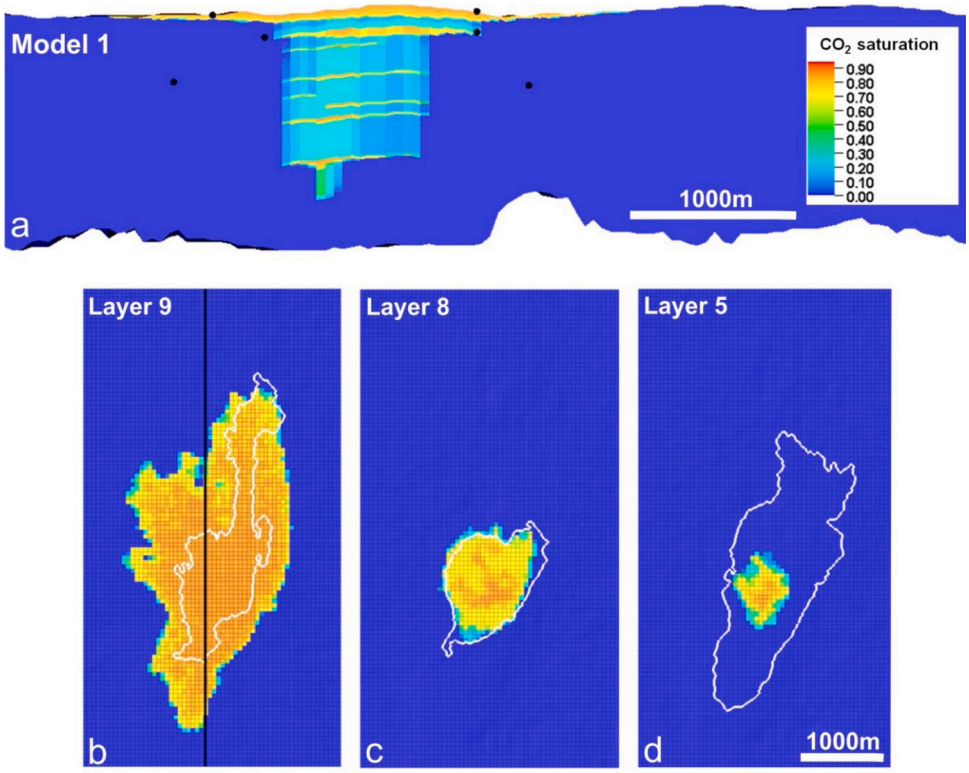

Fig. 12. a) Cross-section through Model 1 at the time of the 2008 survey. b) Predicted CO_2 saturation in Layer 9, black line showing location of cross-section. c) Predicted CO_2 saturation in Layer 8. d) Predicted CO_2 saturation in Layer 5. White polygons in (b) to (d) delimit the CWC as imaged on the seismic data. Black discs in (a) show the CWC limits of the three key CO_2 reflectors on the seismic data.

capillary entry pressure of the chimney to increase the throughput of CO_2 crucially reduces the arrival time of CO_2 at the top of the reservoir, and so fails to match the observed arrival. Note that it might be possible to achieve a match to seismic observations using a non-Darcy flow model in which the CO_2 moved upwards through micro-fractures, with new high permeability pathways evolving over time. Such a hypothetical 'time-variant' permeability effect is not easy to model using conventional Darcy simulators and is not considered further here.

3.6.1.3. Model 3. Time-lapse seismic observations of plume growth show that Layer 9 and Layer 5 grow particularly rapidly, whereas the CO_2 layers beneath Layer 5 slow or stop growing and show diminished reflectivity with time (Figs. 3 and 4). Setting aside the (likely) effects of seismic attenuation, this slowing or cessation of growth and reduced reflectivity could result from decreasing CO_2 saturations in the deeper layers as it migrates progressively more efficiently upwards from the deeper plume to accumulate beneath the shallower mudstones. Model 3 (Fig. 14) therefore modifies Model 2 by increasing the permeability of the four deeper reservoir mudstones (Table 3), removing the need for a shale by-pass pathway.

CO_2 flux to the topmost layer is increased in this model (Fig. 11), but still not sufficiently to replicate the CWC observed on seismic (Fig. 14b). The growth of Layers 5 and 8 is more consistent with seismic observations than Model 2, but their lateral extents comfortably exceed the

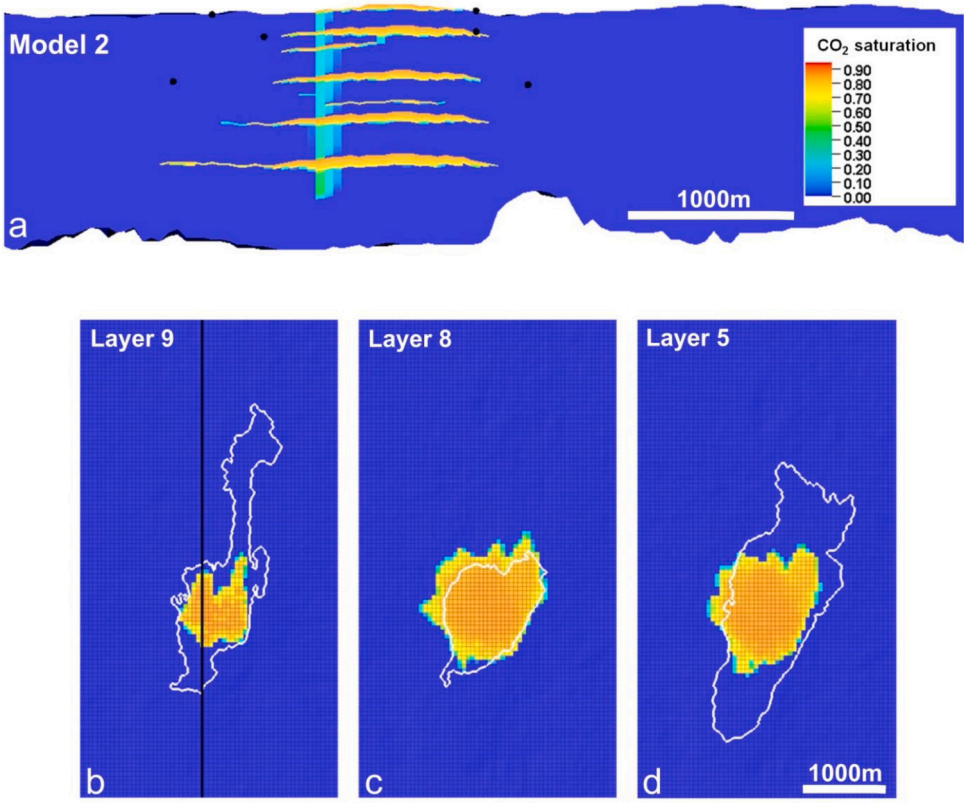

Fig. 13. a) Cross-section through Model 2 at the time of the 2008 survey. b) Predicted CO_2 saturation in Layer 9, black line showing location of cross-section. c) Predicted CO_2 saturation in Layer 8. d) Predicted CO_2 saturation in Layer 5. White polygons in (b) to (d) delimit the CWC as imaged on the seismic data. Black discs in (a) show the CWC limits of the three key CO_2 reflectors on the seismic data.

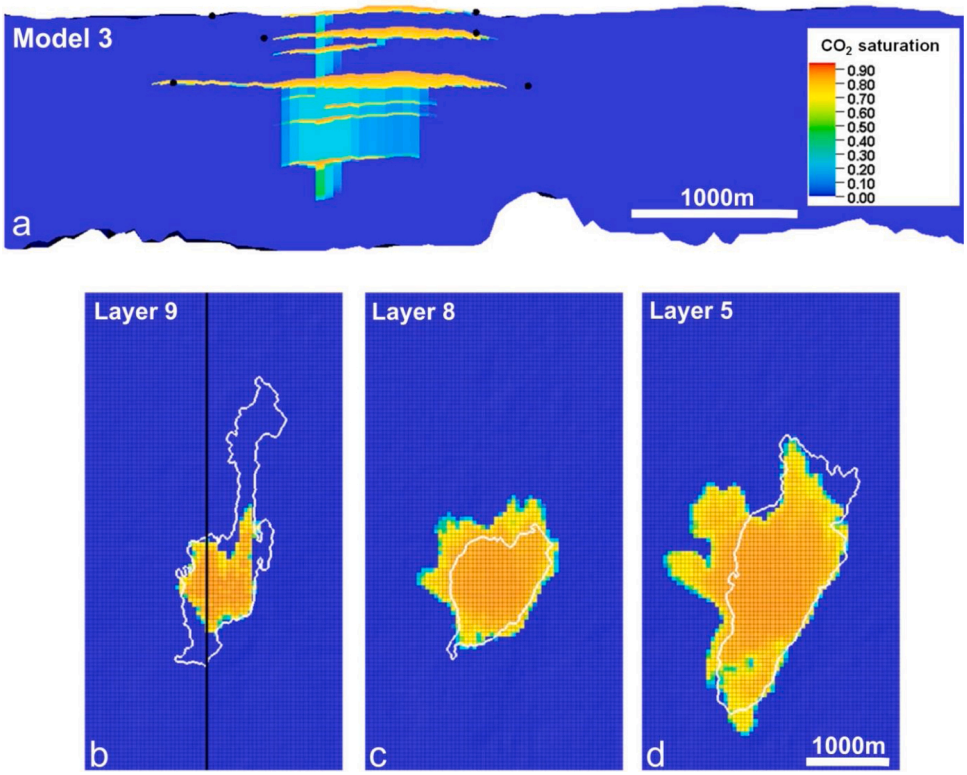

Fig. 14. a) Cross-section through Model 3 at the time of the 2008 survey. b) Predicted CO_2 saturation in Layer 9, black line showing location of cross-section. c) Predicted CO_2 saturation in Layer 8. d) Predicted CO_2 saturation in Layer 5. White polygons in (b) to (d) delimit the CWC as imaged on the seismic data. Black discs in (a) show the CWC limits of the three key CO_2 reflectors on the seismic data.

observed CWC, particularly in the E-W direction (Fig. 14c and d).

3.6.1.4. Model 4. The true vertical extent of the chimney is unclear, so whilst the zone of disrupted reflectivity extends down through most of the plume (Fig. 4), this could well be a seismic imaging or shadowing effect. Model 4 (Fig. 15) therefore introduces a variation to Model 3 by shortening Chimney 1 in a scenario where only Mudstone 8 (the 5-metre mudstone, significantly thicker than the others), has low permeability, and so requires a through-going chimney. The other mudstones are retained as semi-permeable (Table 3). The modelled flux of CO_2 to Layer 9 is markedly increased in this scenario and shows reasonable agreement with observed estimates of Layer 9 vol based on static ponding of CO_2 beneath the topography of the topseal (Fig. 11). The spatial distribution of CO_2 in Layer 9 also shows an improved match to the observed CWC (Fig. 15b), but Layer 8, beneath the 5-metre mudstone, is strongly over-developed (Fig. 15c) because most of the CO_2 has risen through the underlying semi-permeable mudstones to accumulate at this level. Consequently, the deeper CO_2 layers contain significantly less CO_2 and Layer 5 does not remotely match the observed CWC (Fig. 15d).

3.6.1.5. Models 5 and 6. Model 5 (Fig. 16) builds on Model 3 by introducing an additional chimney corresponding to Chimney 2 (Fig. 4) which only breaches the 5-metre mudstone (Mudstone 8) and has the same flow properties as Chimney 1 (Table 3). This increases the flux of CO_2 into Layer 9, providing a good match to observed top layer volume based on calculations assuming static ponding of CO_2 beneath the topography of the caprock (Fig. 11). The fit to the observed CWC for all of the key CO_2 layers is slightly improved although there is still too much E-W spreading of Layers 8 and 5 (Fig. 16c and d).

Model 6 (Fig. 17) modifies Model 5 by extending the second chimney down to and through Mudstone 5. This modification reduces the size of Layer 5 but causes too much CO_2 to pass upwards into Layer 8 and probably also Layer 9 (Figs. 11 and 17). As with the earlier models it is notable that the observed shapes of the layers are poorly reproduced, with too much E-W spreading generally.

A secondary outcome of introducing the second chimney in both Models 5 and 6 is to give two discrete CO_2 accumulations at the top of the reservoir by October 1999, improving the match to the seismic monitor survey (Fig. 18).

3.6.2. Channel fairway models

Whilst it is possible to juggle layer extents and volumes considerably by adjusting the reservoir model in terms of mudstone flow properties and number of chimneys, modelling outcomes are only partially successful in achieving a satisfactory history-match, with clear trade-offs between the growth of the various CO_2 layers. In particular, none of the above models have come close to satisfactorily reproducing the observed spatial extents and shapes of the key plume layers (5, 8 and 9). In order to address this, a further suite of models was developed incorporating enhanced permeability fairways in the reservoir along the lines of those observed and described above (Figs. 6 and 7).

3.6.2.1. Model 7. Model 7 built on Model 5 by incorporating permeability variation into the reservoir model sand units via two horizontal high permeability fairways (see Section 3.5.2). This modification tended to focus CO_2 saturations into the more axial parts of the deeper plume, and increase the CO_2 supply to Chimney 1. One effect of this was to slightly reduce the net flux into Layer 5 and commensurately increase the flux of CO_2 into Layer 9, with an improved match to the observed volumetrics (Fig. 11). A more dramatic effect was a radical improvement in matching the observed CWC for all the layers (Fig. 19), with modelled layer spread much more focussed NNE-SSW and little of the E-W migration evident in the previous models. On the other hand, the model still did not fully replicate the very rapid N-S propagation of Layer 9 (Fig. 19b) and Layer 5 extends too far to the south (Fig. 19d).

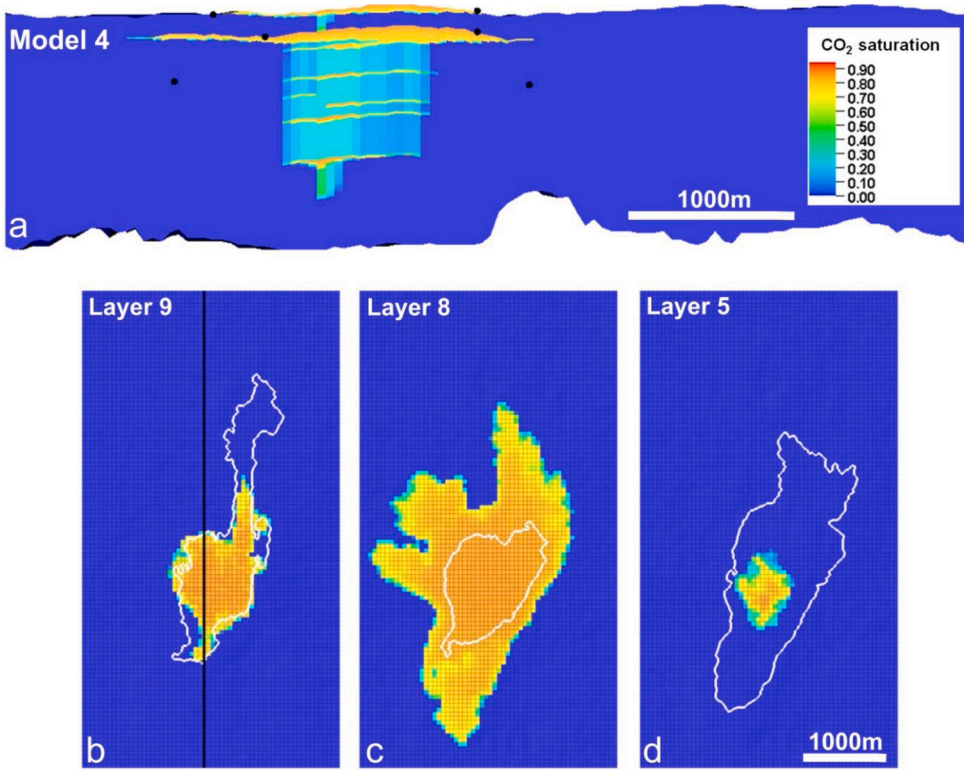

Fig. 15. a) Cross-section through Model 4 at the time of the 2008 survey. b) Predicted CO_2 saturation in Layer 9, black line showing location of cross-section. c) Predicted CO_2 saturation in Layer 8. d) Predicted CO_2 saturation in Layer 5. White polygons in (b) to (d) delimit the CWC as imaged on the seismic data. Black discs in (a) show the CWC limits of the three key CO_2 reflectors on the seismic data.

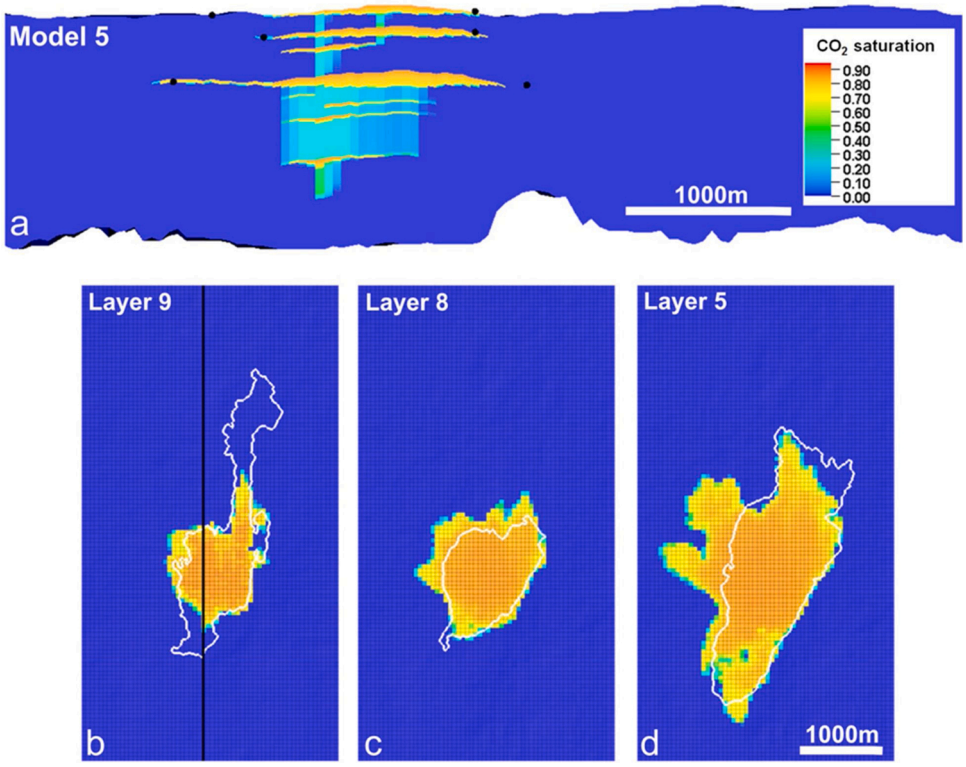

Fig. 16. a) Cross-section through Model 5 at the time of the 2008 survey. b) Predicted CO_2 saturation in Layer 9, black line showing location of cross-section. c) Predicted CO_2 saturation in Layer 8. d) Predicted CO_2 saturation in Layer 5. White polygons in (b) to (d) delimit the CWC as imaged on the seismic data. Black discs in (a) show the CWC limits of the three key CO_2 reflectors on the seismic data.

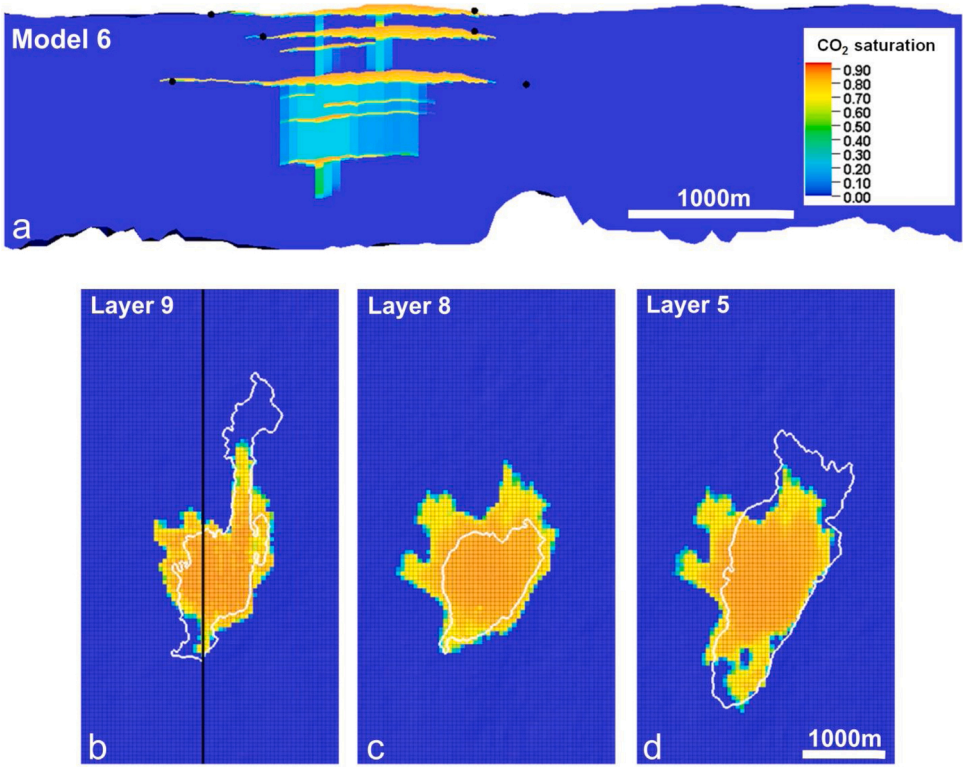

Fig. 17. a) Cross-section through Model 6 at the time of the 2008 survey. b) Predicted CO_2 saturation in Layer 9, black line showing location of cross-section. c) Predicted CO_2 saturation in Layer 8. d) Predicted CO_2 saturation in Layer 5. White polygons in (b) to (d) delimit the CWC as imaged on the seismic data. Black discs in (a) show the CWC limits of the three key CO_2 reflectors on the seismic data.

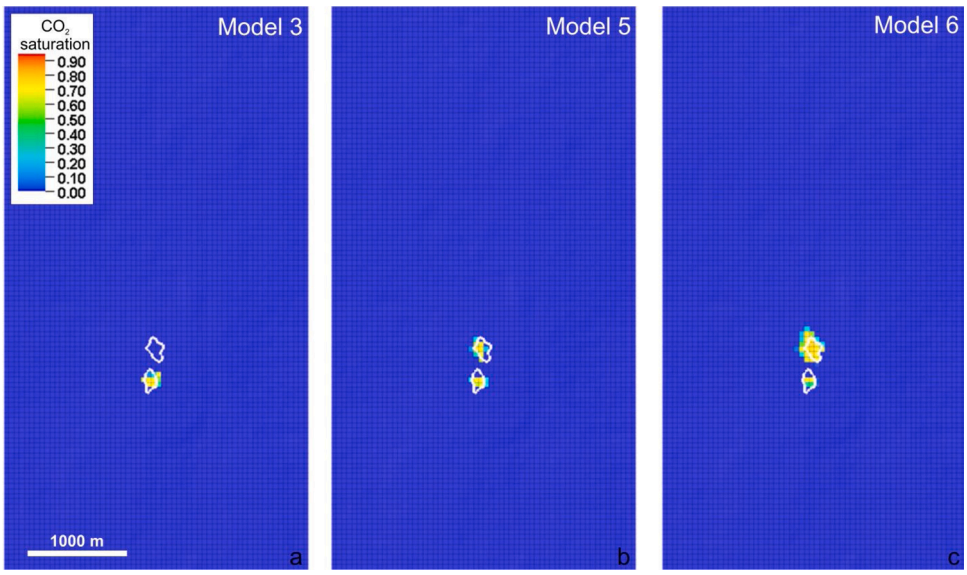

Fig. 18. Modelled CO_2 saturation in Layer 9 at the time of the 1999 survey, just after CO_2 had reached the reservoir top. a) Model 3. b) Model 5. c) Model 6. White polygons show observed extents of the two CO_2 patches at this time.

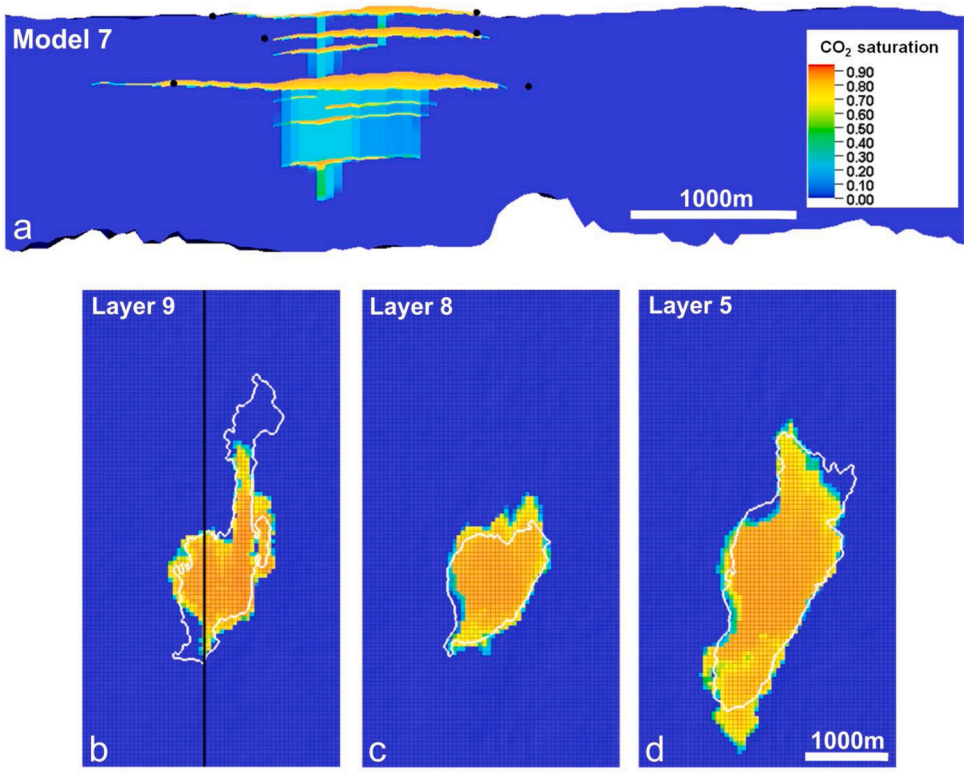

Fig. 19. Cross-section through Model 7 at the time of the 2008 survey. b) Predicted CO_2 saturation in Layer 9, black line showing location of cross-section. c) Predicted CO_2 saturation in Layer 8. d) Predicted CO_2 saturation in Layer 5. White polygons in (b) to (d) delimit the CWC as imaged on the seismic data. Black discs in (a) show the CWC limits of the three key CO_2 reflectors on the seismic data.

3.6.2.2. Models 8, 9 and 10

Models 8, 9 and 10, aim to improve the fit to the observed CWCs at the southern ends of layers 5 and 9 by introducing a third chimney, corresponding to Chimney 3 (Fig. 4). This is guided by information from the seismic data which clearly show a significant accumulation of CO_2 in Layer 7 in the vicinity of Chimney 3 (Fig. 20a), much more extensive than on the Model 7 plume (Fig. 20b).

Model 8 incorporated Chimney 3 with the same flow properties as Chimneys 1 and 2. This however had little effect on Layer 5 and no effect on flux into the overlying plume layers because the thickness of the CO_2 in Layer 5 beneath the chimney was too small to induce buoyancy pressure sufficient to drive flow far enough up the chimney (Fig. 20c).

In Model 9 the permeability of Chimney 3 was assigned reservoir sand properties, effectively introducing a hole into the mudstones. This firstly increased the flux of CO_2 out of Layer 5, significantly decreasing its southerly extent (Fig. 20d). Subsequently most of the CO_2, migrating

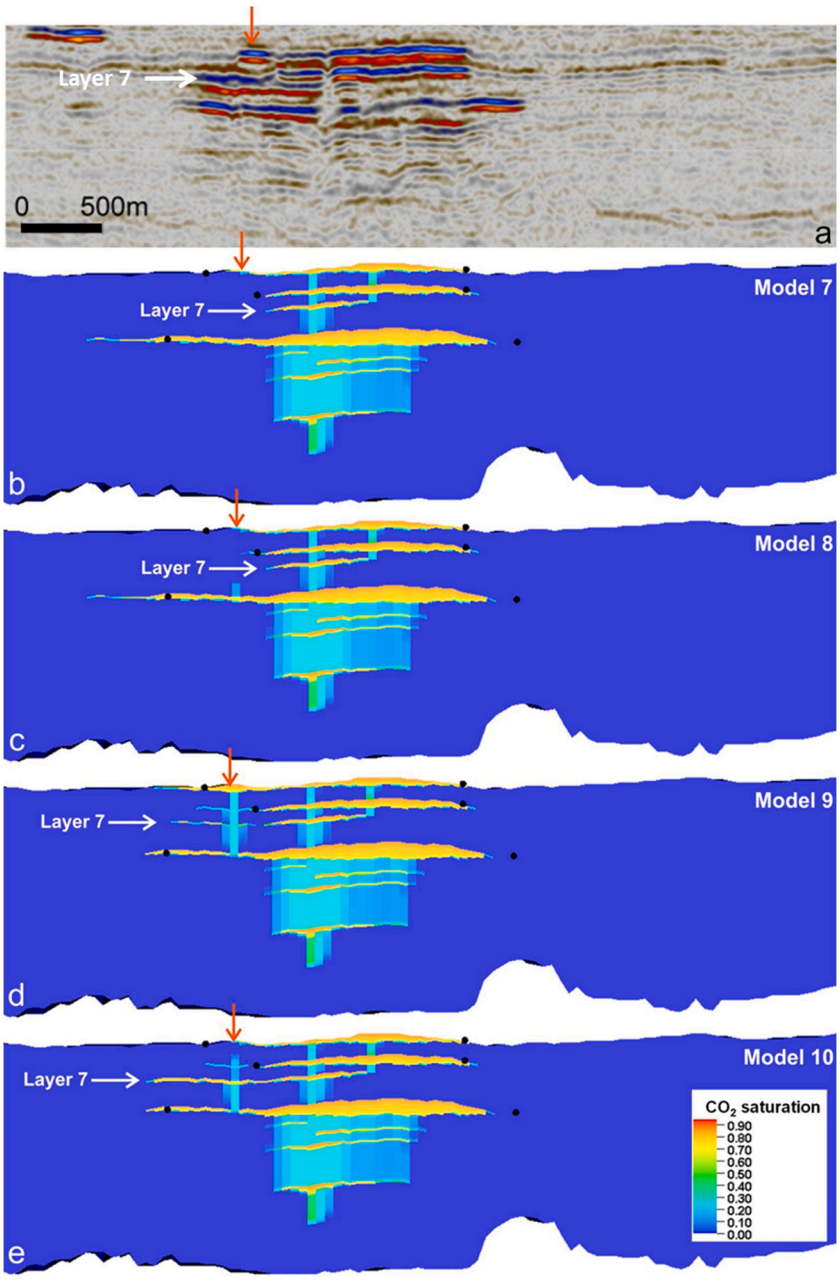

Fig. 20. a) Seismic section from the 2008 survey showing the position and extent of Layer 7. b-e) Co-incident CO_2 saturation profiles through the plume for Models 7 to 10. Red arrows show the location of a small CO_2 accumulation developed in Layer 9 above Chimney 3. Black discs show the CWC limits of the three key CO_2 reflectors on the seismic data.

upwards along the permeable chimney, by-passed Layers 7 and 8 to accumulate at the southern end of Layer 9, increasing its southerly extent (Fig. 20d).

In order to investigate better replicating the observed lateral extent of Layer 7 (Fig. 20a), Chimney 3 in Model 10 was assigned reservoir sand properties at the level of Layer 5 and semi-permeable mudstone properties in the mudstones above. This resulted in an overall better fit to the seismic data, albeit with no CO_2 reaching the topmost sand layer via Chimney 3 until 2010 (Fig. 20e). Adjusting the permeability of the chimney through Mudstone 8 would further improve the fit but that is not really our ultimate aim, which is rather to show that a set of chimneys with baseline pre-cursors helps crucially to reproduce the plume layer evolution. Model 10 also tested the effect of increasing the reservoir permeability outside the model channels by an order of magnitude from 0.1 to 1 Darcy. This did not significantly change the distribution of CO_2 in layers 5, 8 and 9 (c.f. Fig. 20d and e).

In summary, the fit of the three main plume layers for Models 7–10 is generally good, and significantly better than for the earlier models with homogeneous reservoir sand units. Layers 8 and 5 match particularly well (Fig. 21), and the implication from Layer 5 is that permeability heterogeneity (channelling) in the sand is primarily responsible for the elliptical layer shape, rather than topography of the overlying mudstone. Turning to Layer 9, the models produce an appropriate flux of CO_2 at the reservoir top (Fig. 11), but do not replicate the full extent of migration along the N-trending channel. Parallel work on this topic (Williams and Chadwick, 2017; Cowton et al., 2018) has shown that increasing the channel permeability still further can produce a satisfactory fit to the observed migration patterns.

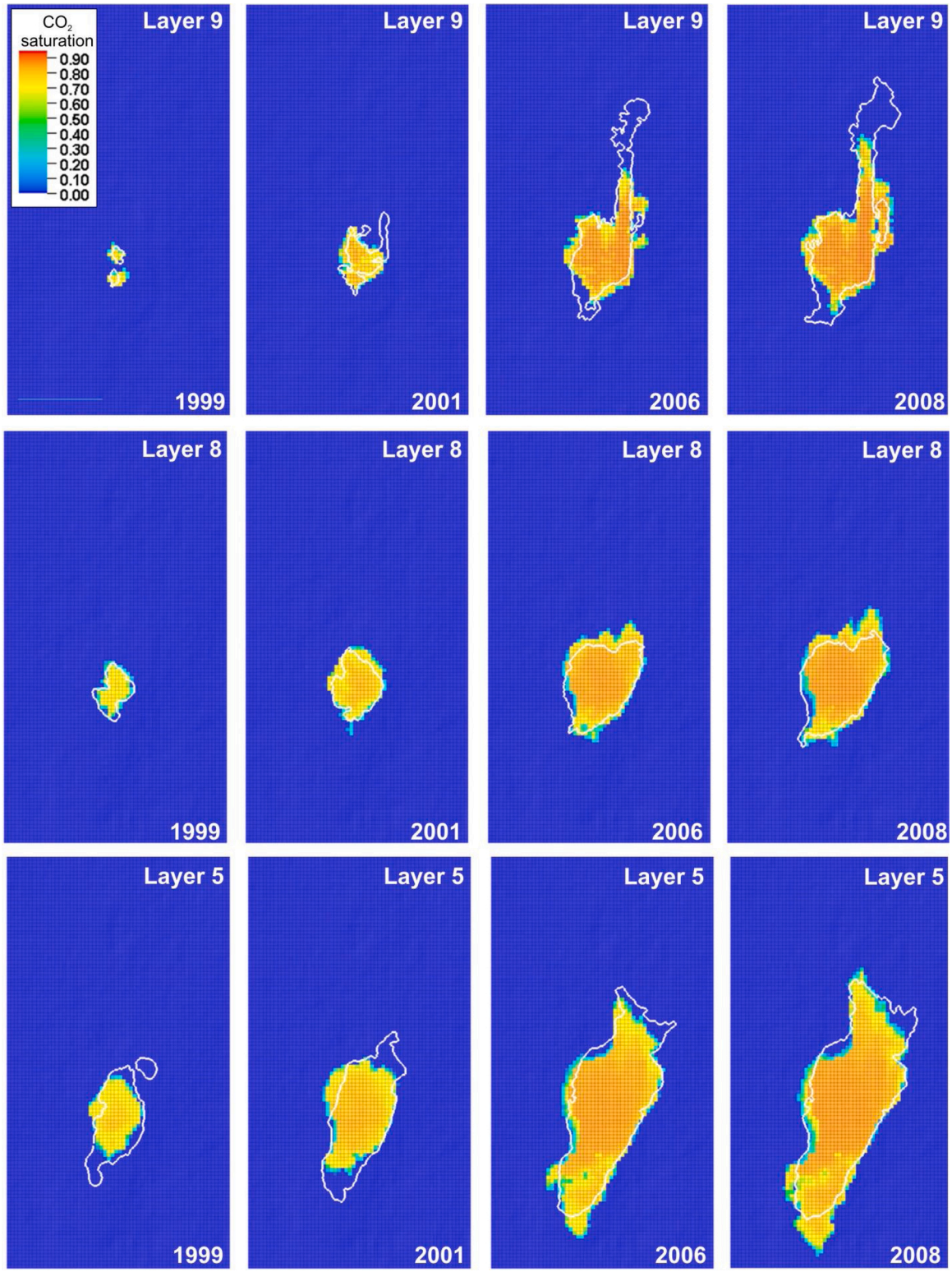

Fig. 21. Model 10: evolution of key layers 9, 8 and 5 in the CO_2 plume. White polygons delimit the CWC observed on time-lapse seismic data.

4. Synthetic seismic modelling

The above model matching depended on fitting the flow models to five parameters interpreted from the time-lapse seismic data: arrival time of CO_2 at the reservoir top; volume evolution of CO_2 in Layer 9; and the lateral extents of Layers 5, 8 and 9. For a more detailed comparison of the flow modelling with the seismic data, synthetic seismograms was generated from flow Model 10.

4.1. Velocity and density relationships

A CO_2 saturation profile was extracted from Model 10 along the line of section used in Figs. 12–20 and velocity and density profiles were computed using Gassmann fluid substitution with a Brie mixing law and

a range of exponents. Brie et al. (1995) derived an empirical mixing law of the form:

$$K_{MIX} = (K_W - K_G) * S_W^e + K_G$$

Where K_{MIX} is the bulk modulus of the water-gas mixture, K_W the bulk modulus of the water phase, K_G the bulk modulus of the gas phase, S_W the water saturation and e an empirical exponent that can be fit to measured velocity-saturation data. The Brie fluid mixing law describes a patchy fluid saturation. When e = 1, the Brie formula reduces to the Voigt average, which represents the upper bound seismic velocity for a gas and water saturated rock (blue curve in Fig. 22). As the exponent, e, increases, the patch size approaches uniform saturation at e = 40. This approximates the Reuss lower bound on seismic velocity for gas-water mixtures (green curve in Fig. 22). Brie et al. (1995) showed that most data they analysed fit the mixing law with calibration constants between e = 2 and e = 5 (orange curves in Fig. 22).

Laboratory ultrasonic velocity measurements made on Utsira Sand core samples over the range of Sleipner reservoir conditions have recently been published (Falcon-Suarez et al., 2018), alongside new theoretical rock physics relating experimentally determined ultrasonic velocities to field-scale seismic velocities (Papageorgiou and Chapman, 2017). These data indicate that Gassmann fluid substitution with Brie mixing and e = 3–5 (Fig. 22) should provide a satisfactory approximation of the seismic velocity - saturation relationship in the Sleipner CO_2 plume and this was used to produce a velocity profile along the line of section together with matching density.

4.2. Synthetic seismograms

A set of 2D finite-difference synthetic seismograms was generated from the calculated velocity and density profiles, with a small amount of random noise added in line with noise levels on the observed data (Fig. 23a, c and e). Comparison with a coincident seismic cross-section (Fig. 23b, d and f) gives a generally good match. A small mismatch is observed around Chimney 3 (Fig. 23) where the arrival time of CO_2 at the reservoir top was not exactly matched in the flow simulation (Section 3.6.3). Imaging in the central parts of the plume around the main chimney is better on the synthetics because an exact stacking velocity model was used and also because seismic attenuation, which would be severe within the chimneys, was not included in the synthetic's computation.

In addition to the plume reflectivity, the seismic velocity reduction caused by substitution of reservoir brine by CO_2 (Fig. 22) also results in a strong cumulative time-shift (velocity pushdown) at the base of the Utsira Sand reflection on the repeat seismic surveys compared with the 1994 baseline (Chadwick et al., 2004). The base Utsira reflection is most clearly seen on the first repeat (1999) survey, because it was much less attenuated than on later surveys. Comparison of mapped time-shifts on the 1999 data with the modelled time-shifts provides an independent test of the saturation distribution and the rock physics model. Flow simulation Model 10 for 1999 incorporating Brie fluid substitution with an exponent of between 3 and 5 provides a very good match to the observed pushdown (Fig. 24).

5. Discussion

The baseline seismic data at Sleipner indicate the presence of a number of vertical and horizontal geological heterogeneities within the Utsira reservoir, some associated with natural fluid (including gas) flow. By including these in our flow modelling, including features outside of the current CO_2 plume envelope, it has proved much easier to match the progressive temporal evolution of key individual plume layers. Layer 9 provides a good example of this: inclusion of the channel fairway identified on the baseline seismic significantly improved the history match with no other modification (Figs. 17 and 19). Layers 8 and 5 show even more dramatically improved history matches by incorporating a simple large-scale channel feature, with distal permeability barriers, into their corresponding sand units (Figs. 17 and 19). We stress again that exact history-matching of each layer is not our intention, although an appropriately designed history matching strategy, applied with respect to a few carefully selected parameters and constrained by the available geological evidence, would help provide additional insights into CO_2 plume dynamics.

Our models are not unique, but the various constraining observations from the evolving CO_2 plume enable the range of possible model variation to be slimmed down markedly. We have moreover deliberately refrained from trying to fit the geological model too closely to the plume images as this would tend to obscure the essential message that the incorporation of relatively simple geological heterogeneity, vertical and horizontal, pays great dividends in understanding the controlling factors on plume evolution. Crucially, these heterogeneities are directly discernible or can be inferred from the baseline seismic and well log data. Additional independent evidence for the presence of channels can be derived directly from the repeat seismic datasets. This is exemplified by recent research into lateral seismic velocity variation in the topmost CO_2 layer (Layer 9) which suggests that velocities in the channels are lower than outside the channels, consistent with the presence of channel sands with higher porosity and permeability (Chadwick et al., 2019).

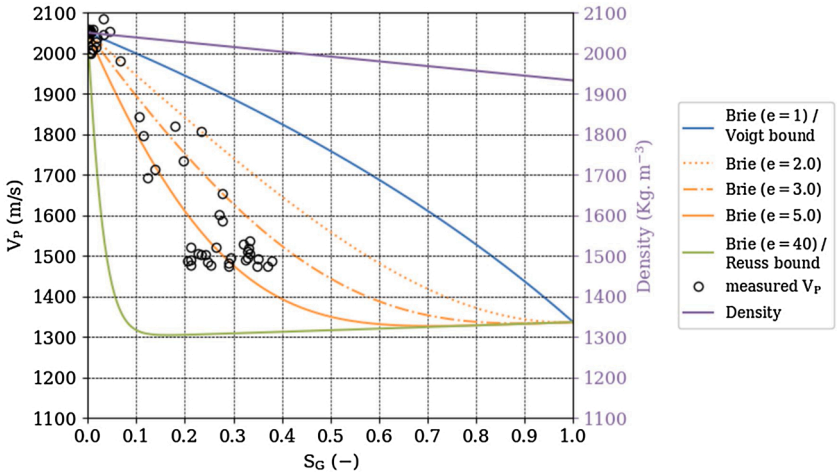

Fig. 22. Rock physics models for the Utsira Sand. Circles show laboratory measurements made on Utsira core (Falcon-Suarez et al., 2018). These measurements indicate that Gassmann fluid substitution with Brie mixing and e in the range 3 to 5 adequately describe the seismic velocity - saturation relationship in the Sleipner CO_2 plume. The synthetic seismic sections in Fig. 23 were generated using a Brie model with e = 5.0 (solid orange line) to relate seismic velocity to CO_2 saturation.

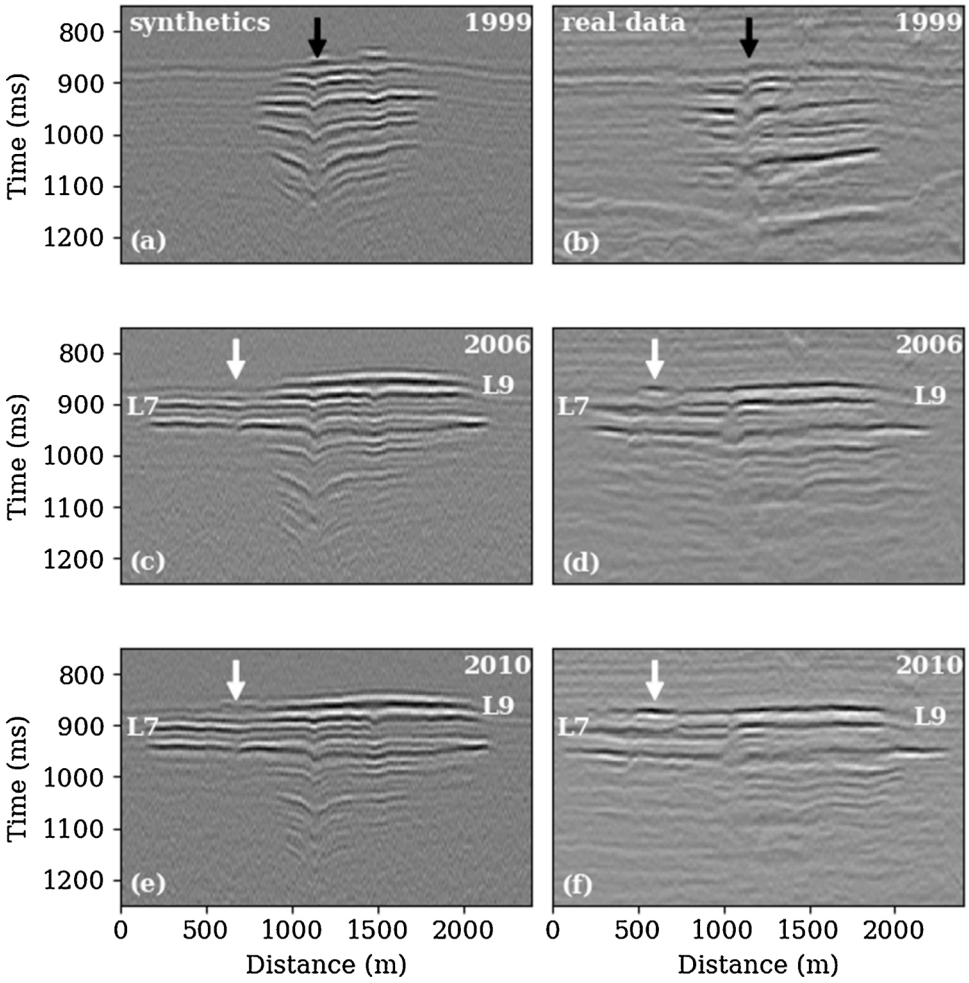

Fig. 23. Comparison of 2D synthetic seismograms (a, c, e) computed along a 2D profile through Model 10 with the coincident inline (b, d, f) from the 1999, 2006 and 2010 time-lapse surveys. The position of the main feeder chimney (Chimney 1) is shown as a thick black arrow in panels a, b. Thick white arrows show the location of a small CO_2 accumulation developed in Layer 9 above Chimney 3.

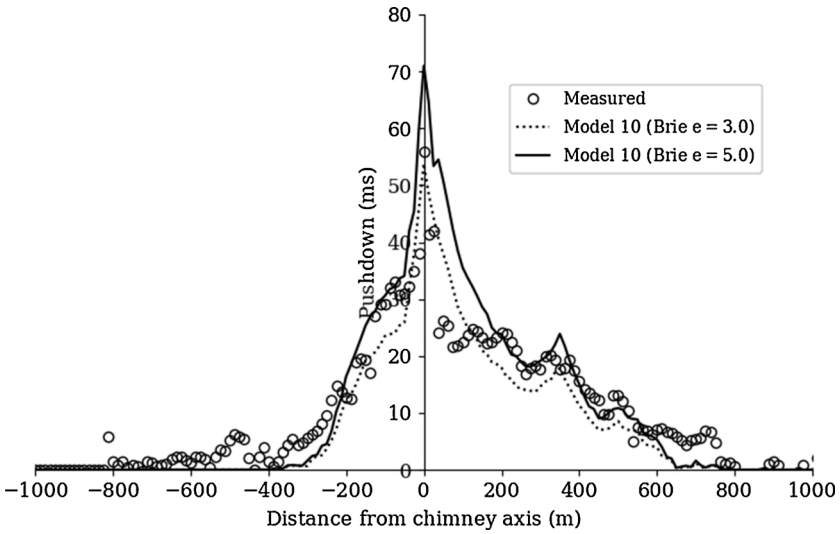

Fig. 24. Comparison of pushdown of the base Utsira Sand reflection on the 1999 time-lapse seismic survey and the corresponding synthetic seismogram computed for a profile through Model 10 for 1999. A Brie fluid mixing law (Fig. 22) was used to compute the bulk modulus of the CO_2-formation brine fluid mixture. Pushdown measurements were extracted from synthetic seismic data computed using Brie exponents of 3.0 (stippled line) and 5.0 (dashed line) for comparison with the measured data.

It is notable that previous work on history-matching Layer 9 using Darcy-based flow simulations with homogeneous reservoir sand has failed to fully replicate the observed evolution of the layer (e.g. Singh et al., 2010; Chadwick and Noy, 2010, 2015; Zhu et al., 2015). This has led a number of authors to suggest models based on alternative physics, invoking processes such as invasion-percolation to improve the match between seismic and simulator (e.g. Cavanagh, 2013). Our findings here suggest that inclusion of more realistic reservoir geology incorporating

simple but evidence-based heterogeneity can remove this modelling issue, and that alternative-physics simulators are not necessary to reproduce the observed plume layer development. Thus, whilst an exact match of Layer 9 has not been achieved (this was not a specific aim of the paper), we believe that such a match would be relatively straightforward with our heterogeneous reservoir model, particularly with full account taken of the exact fluid properties at the reservoir top. We are currently working on this latter aspect, considering the likely elevated temperature of the injected CO_2 and also the presence and effects of significant amounts of methane contamination.

What is particularly striking about the results is that in no case were the flow simulations fine-tuned to match the evolving CO_2 layer shapes, but rather that simple geological heterogeneities inferred from the baseline seismic data tended automatically to improve the plume history-match as they were progressively incorporated. The results are not unique, but their value rather lies in eliminating a range of reservoir permeability options, and in showing that the inclusion of permeability heterogeneity, markedly facilitates whole plume history-matching over a fourteen-year period.

Other storage projects, such as at Snøhvit (Hansen et al., 2013) and Ketzin (Martens et al., 2013) have encountered issues whereby complex permeability structure including distal features outwith the plume envelope have markedly influenced patterns of CO_2 migration and pressure development in the storage reservoir. The findings presented here have wider applicability in emphasising the importance of fully utilising all geological information in accounting for complex permeability structure in storage reservoirs.

6. Conclusions

Baseline (pre-injection) seismic observations on reservoir structure and heterogeneity have been used to develop an improved, but still simple, reservoir model of the Utsira Sand at Sleipner and from this improved flow simulations of the whole Sleipner CO_2 plume. Numerical flow simulations using the revised reservoir model show markedly improved history-matches for key CO_2 layers within the CO_2 plume. The inclusion of up to three vertical permeability conduits, detectable on the baseline seismic data, has improved history matching of CO_2 flux rates and layer development in the uppermost plume. The incorporation of higher permeability channel fairways within the reservoir sand units has radically improved history-matching of CO_2 layer spreading morphology for the main plume layers compared with models that have laterally homogeneous sand properties, and this without any need for detailed layer shape tuning.

Synthetic seismograms of the preferred plume flow model, calibrated by recently acquired laboratory rock physics data from the Utsira Sand, provide strikingly good matches to the observed time-lapse seismic datasets, in terms both of reflectivity and time-shifts. Again, without any manual tuning of layer shapes or thicknesses.

CRediT authorship contribution statement

G.A. Williams: Methodology, Investigation, Writing - original draft. **R.A. Chadwick:** Conceptualization, Writing - review & editing.

Declaration of Competing Interest

The authors declare that they have no known competing financial interests or personal relationships that could have appeared to influence the work reported in this paper.

Acknowledgements

We acknowledge funding from NERC Grant NE/N016386/1 and EPSRC Grants EP/K035878/1 and EP/P026214/1 and also Equinor and the Sleipner partners for access to seismic datasets. The authors publish with permission of the Executive Director, British Geological Survey (NERC). The authors would also like to thank Dr. Anne-Kari Furre of Equinor for her review and helpful comments on the manuscript.

Appendix A. Supplementary data

Supplementary material related to this article can be found, in the online version, at doi:https://doi.org/10.1016/j.ijggc.2021.103260.

References

Alnes, H., Eiken, O., Nooner, S., Sasagawa, G., Stenvold, T., Zumberge, M., 2011. Results from Sleipner gravity monitoring: updated density and temperature distribution of the CO_2 plume. Energy Procedia 4, 5504–5511.

Arts, R.J., Chadwick, R.A., Eiken, O., Thibeau, S., Nooner, S., 2008. Ten years' experience of monitoring CO_2 injection in the Utsira Sand at Sleipner, offshore Norway. First Break 26, 65–72.

Baklid, A., Korbøl, R., Owren, G., 1996. Sleipner Vest CO_2 disposal, CO_2 injection into a shallow underground aquifer. In: SPE Paper 36600, Presented at 1996 SPE Annual Technical Conference and Exhibition. Denver Colorado, USA, 6-9 October 1996.

Brie, A., Pampuri, F., Marsala, A.F., Meazza, O., 1995. Shear Sonic Interpretation in Gas-Bearing Sands, pp. 701–710. SPE 30595.

Cavanagh, A., 2013. Benchmark calibration and prediction of the Sleipner CO_2 plume from 2006 to 2012. Energy Procedia 37, 3529–3545.

Cavanagh, A.J., Haszeldine, R.S., 2014. The Sleipner storage site: Capillary flow modelling of a layered CO_2 plume requires fractured shale barriers within the Utsira Formation. Int. J. Greenh. Gas Control. 21, 101–112.

Chadwick, R.A., Noy, D.J., 2010. History-matching flow simulations and time-lapse seismic data from the Sleipner CO_2 plume. In: Vining, B.A., Pickering, S.C. (Eds.), Petroleum Geology: From Mature Basins to New Frontiers - Proceedings of the 7th Petroleum Geology Conference. Petroleum Geology Conferences Ltd. Published by the Geological Society, London, pp. 1171–1182.

Chadwick, R.A., Noy, D.J., 2015. Underground CO_2 storage: demonstrating regulatory conformance by convergence of history-matched modeled and observed CO_2 plume behavior using Sleipner time-lapse seismics. Greenh. Gas Sci. Technol. 5, 305–322. https://doi.org/10.1002/ghg.1488.

Chadwick, R.A., Zweigel, P., Gregersen, U., Kirby, G.A., Johannessen, P.N., Holloway, S., 2004. Characterisation of a CO_2 storage site: The Utsira Sand, Sleipner, northern North Sea. Energy 29, 1371–1381. Elsevier Science Ltd, Oxford.

Chadwick, R.A., Arts, R., Eiken, O., 2005. 4D seismic quantification of a growing CO_2 plume at Sleipner, North Sea. In: Dore, A.G., Vining, B. (Eds.), Petroleum Geology: North West Europe and Global Perspectives - Proceedings of the 6th Petroleum Geology Conference. Petroleum Geology Conferences Ltd. Published by the Geological Society, London, pp. 1385–1399.

Chadwick, R.A., Williams, G.A., Williams, J.D.O., Noy, D.J., 2012. Measuring pressure performance of a large saline aquifer during industrial scale CO_2 injection: the Utsira Sand, Norwegian North Sea. Int. J. Greenh. Gas Control. 10, 374–388.

Chadwick, R.A., Williams, G.A., White, J.C., 2016. High resolution imaging and characterisation of a CO_2 layer at the Sleipner CO_2 Storage operation using time-lapse seismics. First Break 34, 79–87.

Chadwick, R.A., Williams, G.A., Falcon-Suarez, I., 2019. Forensic mapping of seismic velocity heterogeneity in a CO_2 layer at the Sleipner CO_2 storage operation, North Sea, using time-lapse seismics. Int. J. Greenh. Gas Control. 90, 102793. https://doi.org/10.1016/j.ijggc.2019.102793. ISSN 1750-5836.

Cowton, L.R., Neufeld, J.A., White, N.J., Bickle, M.J., Williams, G.A., White, J.C., Chadwick, R.A., 2018. Benchmarking of vertically - integrated CO_2 flow simulations at the Sleipner Field, North Sea. Earth Planet. Sci. Lett. 491, 121–133.

Duan, Z., Sun, R., Zhu, C., Chou, I.-M., 2006. An improved model for the calculation of CO_2 solubility in aqueous solutions containing $Na+$, $K+$, Ca_2+, Mg_2+, Cl-, and $SO_4$2-. Mar. Chem. 98, 131–139. https://doi.org/10.1016/j.marchem.2005.09.001.

Eidven, T., Riis, F., Rasmussen, E.S., Rundberg, Y., 2013. Investigation of Oligocene to Lower Pliocene deposits in the Nordic offshore area and onshore Denmark. NPD Bulletin 2013 (10), 1–46.

Equinor, 2020. Sleipner 2019 Benchmark Model. Available from. https://doi.org/10.11582/2020.00004. https://co2datashare.org/dataset/sleipner-2019-benchmark-model.

Falcon-Suarez, I., Papageorgiou, G., Chadwick, A., North, L., Best, A., Chapman, M., 2018. CO_2-brine flow-through an Utsira Sand core sample: experimental and modelling. Implications for the Sleipner storage field. Int. J. Greenh. Gas Control. 68, 236–246.

Fenghour, A., Wakeham, W.A., Vesovic, V., 1998. The viscosity of carbon dioxide. J. Phys. Chem. Ref. Data 27, 31–44. https://doi.org/10.1063/1.556013.

Furre, A.-K., Kiaer, A., Eiken, O., 2015. CO_2-induced Seismic Time Shifts at Sleipner.

Furre, A.-K., Ringrose, P., Santi, A.C., 2019. Observing the invisible - CO_2 feeder chimneys on seismic time-lapse data. In: European Association of Geoscientists & Engineers81st EAGE Conference and Exhibition 2019, Vol. 2019. https://doi.org/10.3997/2214-4609.201901646. No. 1, pp. 1-5.

Gershenzon, N.I., Ritzi, R.W., Dominic, D.F., Soltanian, M., Mehnert, E., Okwen, R.T., 2015. Influence of small-scale fluvial architecture on CO_2 trapping processes in deep brine reservoirs. Water Resour. Res. 51, 8240–8256. https://doi.org/10.1002/2015WR017638.

Gregersen, U., Michelsen, J.C., 1997. Stratigraphy and facies distribution of the Utira Formation and the Pliocene sequences in the northern North Sea. Mar. Pet. Geol. 14 (7/8), 893–914.

Hansen, O., Gilding, D., Nazarian, B., Osdal, B., Ringrose, P., Kristoffersen, J.-B., Eiken, O., Hansen, H., 2013. Snøhvit: the history of injecting and storing 1Mt CO_2 in the Fluvial Tubåen Fm. Energy Procedia 37, 3565–3573.

Harrington, J.F., Noy, D.J., Horseman, S.T., Birchall, D.J., Chadwick, R.A., 2010. Laboratory study of gas and water flow in the Nordland Shale, Sleipner, North Sea. In: Grobe, M., Pashin, J.C., Dodge, R.L. (Eds.), Carbon Dioxide Sequestration in Geological Media – State of the Science, AAPG Studies in Geology. AAPG, pp. 521–543.

Hassanzadeh, H., Pooladi-Darvish, M., Elsharkawy, A.M., Keith, D.W., Leonenko, Y., 2008. Predicting PVT data for CO2-brine mixtures for black-oil simulation of CO2 geological storage. Int. J. Greenh. Gas Control. 2, 65–77. https://doi.org/10.1016/S1750-5836(07)00010-2.

Kennett, C., 2008. Evaluation of internal geometries within the Miocene Utsira Formation to establish the geological concept of observed CO_2 responses on 4D seismic in the Sleipner area, North Sea. MSc Petroleum Geoscience. Imperial College London, p. 66 p..

Lindeberg, E., Zweigel, P., Bergmo, P., Ghaderi, A., Lothe, A., 2001. Prediction of CO_2pattern improved by geology and reservoir simulation and verified by time-lapse seismic. Proceedings of the 5th International Conference on Greenhouse Gas Control Technologies 372–377.

Martens, S., Liebscher, A., Moller, F., Henninges, J., Kempka, T., Luth, S., Norden, B., Prevedel, B., Szizybalski, A., Zimmer, M., Kuhn, M., Ketzin, G., 2013. CO_2 storage at the Ketzin pilot site, Germany: fourth year of injection, monitoring, modelling and verification. Energy Procedia 37, 6434–6443.

Papageorgiou, G., Chapman, M., 2017. Wave propagation in rocks saturated by two immiscible fluids. Geophys. J. Int. 209, 1761–1767 https://doi.org/10.1093/gji/ggx128.

Saadatpoor, E., Bryant, S.L., Sepehrnoori, K., 2010. New trapping mechanism in carbon sequestration. Transp. Porous Med. 82, 3–17. https://doi.org/10.1007/s11242-009-9446-6.

Singh, V.P., Cavanagh, A., Hansen, H., Nazarian, B., Iding, M., Ringrose, P.S., 2010. In: Reservoir Modelling of CO_2 Plume Behaviour Calibrated Against Monitoring Data from Sleipner, Norway. Society of Petroleum Engineers, SPE. https://doi.org/10.2118/134891-MS. SPE-134891-MS.

Span, R., Wagner, W., 1996. A new equation of state for carbon dioxide covering the fluid region from the triple-point temperature to 1100 K at pressures up to 800 MPa. J. Phys. Chem. Ref. Data 25, 1509–1596.

Spycher, N., Pruess, K., 2005. CO_2-H_2O mixtures in the geological sequestration of CO2. II. Partitioning in chloride brines at 12-100 C and up to 600 bar. Geochim. Cosmochim. Acta 69, 3309–3320. https://doi.org/10.1016/j.gca.2005.01.015.

Van der Meer, L.G.H., Arts, R.J., Peterson, L., 2000. Prediction of migration of CO_2 injected into a saline aquifer: Reservoir history matching to a 4D seismic image with a compositional Gas/Water model. In: Williams, D.J., Durie, R.A., McMullan, P., Paulson, C.A.J., Smith, A.Y. (Eds.), Greenhouse Gas Control Technologies. CSIRO Publishing, Collingwood, Australia, pp. 378–384.

Vesovic, V., Wakeham, W.A., Olchowy, G.A., Sengers, J.V., Watson, J.T.R., Millat, J., 1990. The transport properties of carbon dioxide. J. Phys. Chem. Ref. Data 19, 763–808. https://doi.org/10.1063/1.555875.

White, J.C., Williams, G., Chadwick, A., Furre, A.-K., Kiaer, A., 2018. Sleipner: The ongoing challenge to determine the thickness of a thin CO_2 layer. Int. J. Greenh. Gas Control. 69, 81–95.

Williams, G.A., Chadwick, R.A., 2012. Quantitative seismic analysis of a thin layer of CO_2 in the Sleipner injection plume. Geophysics 77, R245–R256.

Williams, G.A., Chadwick, R.A., 2017. An improved history-match for layer spreading within the Sleipner plume including thermal propagation effects. Energy Procedia 114, 2856–2870.

Zaytsev, I., Aseyev, G., 1992. Properties of Aqueous Solutions of Electrolytes. CRC Press.

Zhu, C., Zhang, G., Lu, P., Meng, I., Ji, X., 2015. Benchmark modelling of the Sleipner CO_2 plume: calibration to seismic data for the uppermost layer and model sensitivity analysis. Int. J. Greenh. Gas Control. 43, 233–246.

Zweigel, P., Arts, R., Lothe, A.E., Lindeberg, E., 2004. Reservoir geology of the Utsira Formation at the first industrial-scale underground CO_2 storage site (Sleipner area, North Sea). In: Baines, S.J., Worden, R.H. (Eds.), Geological Storage of CO2, 233. Geological Society, London, pp. 165–180. Special Publication.